Paleoenvironmental variations during the Late Cambrian: implications from Zn isotopes and I/(Ca+Mg) ratios

By

Luisa GONZÁLEZ ROBACIO

A thesis submitted to the

School of Graduate Studies

In partial fulfilment of the requirements for the degree of

Master of Science

Department of Earth Sciences

MEMORIAL UNIVERSITY OF NEWFOUNDLAND

July 2023

St. John’s, Newfoundland

Abstract

The Upper Cambrian at the Martin Point section partially spans the coeval Tuckers Cove (Shallow Bay Formation) and the Martin Point (Green Point Formation) members of the Cow Head Group of western Newfoundland (eastern Laurentia), Canada. These units comprise alternating shale, minor conglomerate beds and limestone rhythmites of a toe-of-slope apron. Earlier studies of the C-isotope profile, based on the lime mudstone interbeds, documented global negative $\delta^{13}C_{carb}$ shifts (from old to young: NL1, NL2, HERB) correlated with the lowermost *Proconodontus posterocostatus*, *Proconodontus muelleri* and base of *Eoconodontus notchpeakensis* conodont zones, respectively. Samples were extracted from the most micritic spots, where the micritic to near-micritic grain size ($\leq$ 4 µm−10 µm) and fabric retention confirm petrographic preservation. Insignificant correlations of diagenetic proxies with their environmental counterparts support high degree of geochemical preservation. The zinc-isotope ($\delta^{66}Zn$) signatures (0.09 – 0.73 ‰ JMC Lyon) and iodine-to-calcium-plus-magnesium (I/(Ca+Mg)) ratios (0.02 – 0.48 µmol/mol) vary consistently throughout the studied events and were employed to shed light on paleoenviromental conditions. The decrease in $\delta^{66}Zn$ values seems to denote inhibition of bioproductivity in a dysoxic water column, consistent with warm and humid climate during general transgressive settings and shoaling of organic matter into the shallow environment. On the contrary, slight increases in $\delta^{66}Zn$ (<0.8 ‰ JMC Lyon) might reflect weak bioproductivity and possible influence of carbonate weathering input during minor fluctuations (episodic falls) in sea level during the main course of the transgression. The low I/(Ca+Mg) ratios (< 0.5 µmol/mol) reinforce this interpretation, suggesting general dysoxic settings along the entire section.

General Summary

The Martin Point section at Martin Point, western Newfoundland, Canada, exposes rocks that deposited as a toe-of-slope apron during the Late Cambrian and which are part of the Tuckers Cove Member of the Shallow Bay Formation and the Martin Point Member of the Green Point Formation of the Cow Head Group (eastern margin of the Laurentia paleocontinent). Earlier studies of the C-isotope concentrations in the finer-grained carbonate strata documented global negative shifts (named from old to young: NL1, NL2, HERB) correlated with fossil zones (conodont zones). Samples were extracted from the finer-grained spots, where grain size, fabric retention, and low correlation of the elemental and isotopic concentrations confirm that these samples are well preserved and retain at least near-primary geochemical signatures. The decreasing values of the zinc-isotopes throughout the events seem to denote inhibition of bioproductivity in a dysoxic water column, consistent with warm and humid climate conditions during a rise in the sea level, and delivery and emplacement of organic matter into the shallow environment. Slight increases in the zinc-isotope signature suggest weak bioproductivity and possible influence of carbonate weathering input during minor episodic falls in the sea level during a general rise. Low I/(Ca+Mg) ratios reinforce this interpretation, suggesting general dysoxic settings along the entire section.

Acknowledgements

I thank supervisor Dr. Karem Azmy for his professional guidance, corrections and the chance to pursue this research study. This project was supported by funding from the School of Graduate Studies of Memorial University of Newfoundland and from Mitacs Canada (to Dr. Karem Azmy).

The author also wishes to acknowledge Drs. Svend Stouge and Bleuenn Gueguen (Institut Universitaire Européen de la Mer, France) for technical assistance in collecting the samples and chemical analyses, respectively.

Last but not least, I would like show my gratitude to my family and friends, who encouraged and supported me from a distance while I was studying in a foreign country. Also, to the second family and colleagues I met in St. John's, who warmly welcomed me and made this an even more enriching experience. I thank God for His ways.

Table of Contents

List of Tables

List of Figures

List of Appendices

Co-authorship Statement

This thesis is presented in a traditional style and consists of six chapters. Chapter I introduces the topic, the two main proxies to be utilized as trackers of paleoenvironmental conditions and outlines the main objectives of the study. Chapter II locates the investigated succession within its geological setting as sedimentary rocks part of the Humber Arm Allochthon of western Newfoundland, describes the lithology conforming the Cow Head Group and, specifically, the Tuckers Cove Member of the Shallow Bay Formation and the Martin Point Member of the Green Point Formation, and elaborates on the biostratigraphic framework of the section. Chapter III describes sample collection, treatment and analyses procedures to obtain the elemental and isotopic concentrations of the carbonates. The results are described in Chapter IV, and the discussion, in Chapter V, explores and proposes possible causes for the variations of the concentrations of the proxies during the events NL1, NL2 and HERB, such as bioproductivity, redox conditions, terrigenous inputs and climate. The final chapter (Chapter VI) summarizes the conclusions of this research project.

The mainframe of the research was designed by Dr. Karem Azmy. As co-author, Dr. Karem Azmy guided the research progress, advised me on analyzing and interpreting the data, and corrected the manuscript prior to submission. As the primary author, I was responsible for reviewing the literature, performing laboratory work, analyzing and interpreting the data, preparing the manuscript and all aspects of the thesis, apart from the sample collection and elemental and isotopic analyses of the samples, which were performed by Drs. Svend Stouge and Bleuenn Gueguen, respectively. The latter also provided the methodology utilized for the elemental and isotopic analyses.

Chapter I

Introduction and Objectives

Geochemistry and chemostratigraphy of carbonates have been proven very reliable tools in understanding the paleoenvironmental and paleoclimatic aspects of the Earth's history. The fast-advancing analytical techniques make it possible for researchers to detect variations in the chemical compositions of rocks and minerals at high-resolution. In particular, geochemistry in carbonates is progressively proving to be a valuable tool for this aim, as their composition appears to record that of the seawater from which they precipitated. This allows to infer parameters such as salinity, temperature, density, pH, fluvial influx, weathering rate, paleoredox, effect of diagenesis or bioproductivity, employing elements and stable isotopes which include C, O, B, Ce, Cr, and Mo (e.g., Kasemann et al., 2009; Nakada et al., 2013; Rostovtseva and Kuleshov, 2016; D'Arcy et al., 2017; Scholz et al., 2017; Niu et al., 2018).

Recently, the Zn stable isotopes (δ^{66}Zn signatures) of carbonates have been utilized to trace ancient seawater composition (e.g., Pichat et al., 2003; Yan et al., 2019; Zhao et al., 2021) and paleoenvironmental conditions, such as bioproductivity (e.g., Kunzmann et al., 2013), surface runoff (e.g., Kunzmann et al., 2013) and redox conditions (e.g., Mavromatis et al., 2019).

Zinc is an essential biological nutrient (micronutrient) and is therefore depleted from the surface seawater due to uptake in the photic zone and regenerated at depth, through oxidation of organic matter by bacterial activity and the dissolution of sinking particles (Bruland, 1980). The Zn isotopes are especially fractionated by dissolved phosphate and carbonate (Pons et al., 2013) when assimilated and removed by primary producers (Pichat et al., 2003). Earlier studies (Mavromatis et al., 2019) also suggest variability in the

fractionation factor between calcite and seawater due to pH. Generally speaking, Zn is an ideal substitution for Ca^{2+} (Reeder et al., 1999) and is incorporated into the crystal lattice of carbonate minerals in trace amounts. The $\delta^{66}Zn$ signature in carbonate minerals may record the isotope composition of seawater (Pichat et al., 2003; Yan et al., 2019; Zhao et al., 2021), but it is necessary to assess the effect of diagenesis on the material to confirm that the signatures are primary or at least near-primary (Hohl et al., 2015).

Iodine is present in seawater as the thermodynamically stable dissolved forms iodate (IO_3^-) and iodide (I^-) (Wong and Brewer, 1977). As iodine is highly redox-sensitive, its speciation change iodide/iodate has been proposed as a redox proxy (Liss et al., 1973). It occurs mainly as iodate under well-oxygenated conditions (Truesdale and Bailey, 2000), however, as the water column oxygen concentrations decrease, the iodate is reduced to iodide (Bowman et al., 2021), which dominates in anoxic basins and porewaters (Wong and Brewer, 1977).

Iodate is the sole anion incorporated into the carbonate structure (Lu et al., 2010), as it partially substitutes $CaCO_3$, while iodide cannot enter this mineral, likely due to the large ionic radius of iodide relative to iodate (Zhou et al., 2015). Iodate accumulates in planktonic and benthic marine calcifiers and, ultimately, trace amounts compose carbonate rocks (Fuge and Johnson, 1986). Iodine-to calcium ratio (I/Ca) is independent of I^- in parent waters, but it is affected by the IO_3^- concentration in water in a linear relationship (Lu et al., 2010). Therefore, the ratio, expressed as I/(Ca+Mg), appears as a useful tracer in carbonates for redox conditions in the geological past.

The Cambrian was a period with an overall warm temperature and progressive sea-level rise, but marked by brief episodes of abrupt changes (e.g., Babcock et al., 2015). These events seem to be recorded in the $\delta^{13}C$ values of carbonates and, during the Furongian,

distinctive global shifts have been documented, including the post-SPICE (post-Steptoean Positive Carbon Isotope Excursion; Li et al., 2006; Azmy, 2019b) and the HERB (Hellnmaria-Red Tops Boundary; Miller et al., 2011; Li et al., 2017; Azmy, 2019b) events. The currently investigated section at Martin Point (western Newfoundland, Canada) spans the post-SPICE and HERB events.

The main objectives of the current study are:

1. To evaluate the preservation of the Zn isotope and I/(Ca+Mg) signatures retained in the Martin Point carbonates.
2. To investigate the variations of Zn isotopes and I/(Ca+Mg) ratios in the late Cambrian ocean water to reconstruct the paleoenvironmental conditions during that time interval.
3. To shed light, when applicable, on the variations in the paleoredox conditions.

Chapter II

Geologic Setting and Biostratigraphic Framework

2.1 Geological Setting

Western Newfoundland is the northeast extension of the Appalachian mountain range in Canada (Fig. 1) that forms a part of the Humber Zone tectostratigraphic terrane (Williams, 1978) and has the best-preserved successions of the early Paleozoic margin of Laurentia (North America). The successions overlie unconformably the Grenvillian basement and record parautochthonous sedimentary units from Cambrian to Silurian and allochthonous units containing sedimentary, igneous, and metamorphic rocks (James and Stevens, 1986; Quinn et al., 1999; Cooper et al., 2001). The transported rocks were structurally emplaced onto the Laurentian margin during the Taconian and Acadian orogenies and constitute the Humber Arm Allochthon in the south of western Newfoundland, of which the sedimentary rocks are called the Humber Arm Supergroup (Stevens, 1970).

During the Neoproterozoic rifting of Rodinia, seafloor spreading between Laurentia and west Gondwana resulted in the opening of the Iapetus Ocean (Cawood et al., 2001) and the establishment of the Laurentian margin (Waldron et al., 1998), which developed during latest Precambrian to early Cambrian. A succession of variable thickness of terrestrial to arkosic sandstones, conglomerates, graywackes, quartzites and local thick volcanic units and mafic dykes deposited during rifting and continental breakup (Williams and Hiscott, 1987). On the other hand, the overlying assemblage shows a more homogeneous thickness, lateral continuity and represents a marine succession deposited during the thermal subsidence of the margin and development of a carbonate platform.

In western Newfoundland, the Bateau, Lighthouse Cove, and Bradore formations (Labrador Group) embody the synrift rocks, the transition from rift to passive margin lying within the Bradore Formation (Allen et al., 2010) or at its base (Cawood et al., 2001). The Forteau Formation from the same group represents the thermal subsidence of the margin and, thus, an extensive marine transgression (Williams and Hiscott, 1987) on a mainly siliciclastic shelf. During the Middle to Late Cambrian, the high-energy carbonate platform of the Port au Port Group developed, followed by the St. George Group's low-energy carbonate platform (Early Ordovician) and a carbonate bank belonging to the Table Head Group (Middle Ordovician), which determines the final phase of the passive-margin sequence (Stenzel et al., 1990).

The allochthonous sedimentary rocks of the Humber Arm Supergroup span Early Cambrian to Middle Ordovician and are divided into two deep-water units: the Curling and the Cow Head Group (Fig. 2). They register the passive continental margin and foredeep environments, and a record of rifting, continental margin subsidence, and continent-arc collision (Waldron and Palmer, 2000). The Cow Head Group was deposited along the continental southeast-dipping slope as debris shed from the platform into deeper water (Williams and Hiscott, 1987; Lacombe et al., 2019), forming an extensive sedimentary apron with a proximal-distal polarity from northwest to southeast, which translates into the Shallow Bay and the Green Point formations, respectively (James and Stevens, 1986).

The Humber Arm Allochthon rocks are disposed as a series of thrust slices (White and Waldron, 2018) accreted onto the Laurentian margin, as the Taconian orogenesis began in the Early Ordovician with westward thrusting, signalling the first effect of the closure of the Iapetus Ocean in western Newfoundland (Waldron et al., 1998). The Cow Head Group is stratigraphically overlain by flysch due to the development of a foreland basin (Quinn, 1992). Deformation generated by the Acadian orogenesis during the Devonian was imprinted, in a

later stage, on the Taconian thrusts and melange belts (Cousineau and Tremblay, 1993; White and Waldron, 2018).

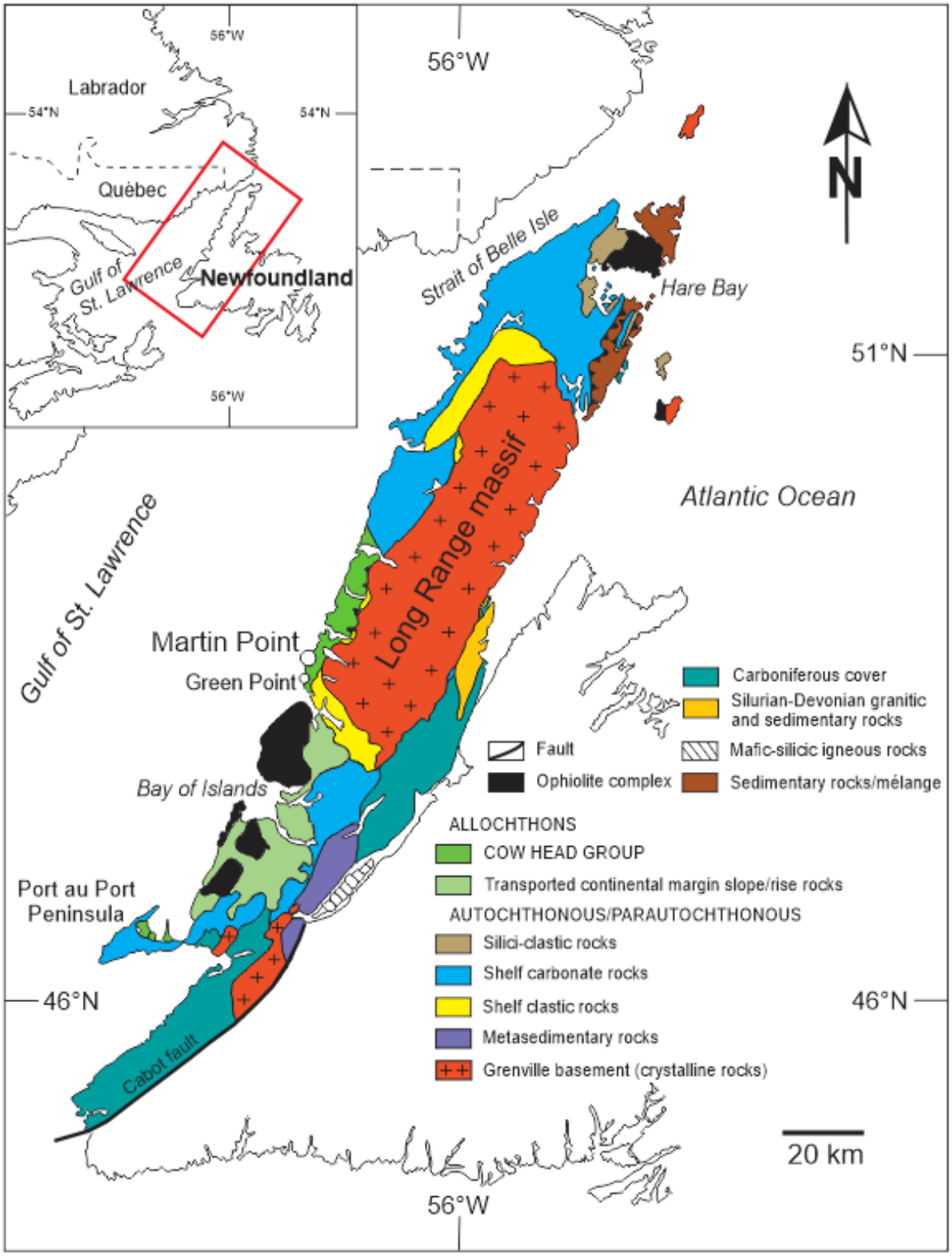

Fig. 1. Location map showing surface geology and the study area in western Newfoundland, Canada (modified from James and Stevens, 1986; Cooper, 2001).

2.2 Lithostratigraphy

The Cow Head Group lithostratigraphy (Fig. 2) was extensively described and discussed by James and Stevens (1986). The unit is dominated by rhythmites deposited at the foot of a continental slope, as a mixture of fine-grained hemipelagites and sediment gravity flows, which consistof alternations of shales, siltstones, and limestones.

The shales are laminated and vary from black to dark grey and green due to deposition under anoxic to dysoxic conditions, or appear red and bioturbated. The dolomitic siltstones and silty dolomites are buff weathering and combine both detrital and diagenetic deposits. Interlaminations of shales and siltstone occur in association with turbidite deposits (Coniglio, 1985; Bouma, 1962; Stow and Shanmugam; 1980).

Carbonates occur as ribbon (alternations of interbeds of carbonates and argillaceous layers with similar thickness) or parted limestones (argillaceous layers are significantly thinner) (James and Stevens, 1986). These rhythmites appear like planar, lumpy beds or nodules in shale and their textures include lime mudstones (Dunham, 1962), graded calcisiltite, and rippled calcarenite.

Quartzose calcarenites show coarse to very coarse grains with rounded and spherical shapes (typical eolian quartz), and ooids whereas algal bioclasts conform mainly the allochems. These rocks can be massive because of grain flows, graded as in turbidite deposits or disposed as caps on top of conglomerates. Coniglio (1985) proposed that the turbidite deposits are a result of high-density turbidity currents.

The Cow Head Group (Fig. 2) comprises two coeval formations: the Shallow Bay Formation, of which the Tuckers Cove Member constitutes the lower part of the currently investigated section at Martin Point, and the overlying Green Point Formation, of which the

Martin Point Member constitutes the upper part of the investigated section. These two members formed when the deposition of the sediment apron changed to mainly quartz-rich calcarenites with shales and minor conglomerates (Tuckers Cove Member), grading distally into Martin Point Member lithology, as the sand wedge was considerably widespread.

The proximal Shallow Bay Formation is 100 to 300 m-thick and composed of a sequence of limestone conglomerate and calcarenite with interbedded limestone and shale in the upper part. The Tuckers Cove Member is the uppermost member of the Shallow Bay Formation and consists of interbedded quartzose calcarenite, graded stratified conglomerate to occasional boulder conglomerate, minor parted to ribbon limestone separated by green calcareous shale, sandstone, buff-weathering, well-laminated or rippled dolomitic siltstones, and thin black shale.

The texture of the parted to ribbon limestone is commonly mudstone. They contain radiolarian and pelsparite microlaminations that vary between silt and fine sand in grain size. Calcarenites with medium to coarse grain and rippled or cross-laminated sedimentary structures are less frequent.

The Tuckers Cove Member shows massive or crossbedded quartzose calcarenite units or thin layers that are disposed within the shales or small channels. Rounded peloids, intraclasts, and fragments of fossils constitute the allochems, which are medium- to very coarse grain in size. The sediments are layered, finely interlaminated, or mixed with silt and may contain small amounts of dolomite and phosphate.

The occurrence of the quartzose calcarenites decreases in the upper half of the Tuckers Cove Member, while the parted and ribbon limestone and conglomerates become more frequent in the investigated Martin point section and conglomerates only represent a minor portion of the sequence (James and Stevens, 1986). Kindle and Whittington (1958)

suggested that the conglomerates are the result of slumping processes whereas Hubert et al. (1977) proposed that debris flow is the responsible mechanism.

On the other hand, the distal Green Point Formation occurs as fine-grained facies that are 400 to 500 m thick. The strata are mostly green, red, and minor black shale with occasional conglomerate and ribbon-to-parted limestone. The Martin Point Member is the basal unit with a thickness ranging from 100 to 150 m and composed of green and black shale with partings of thin buff-weathering siltstone and calcareous sandstone, layers of ribbon and parted limestone, and scarce thin conglomerate beds.

The siltstones, which are interlaminated with the shales, are distinguishably rippled and their surfaces may show tracks and trails. They contain ferroan dolomite and when the amount is approximately 2/3 they are called silty dolostones. The limestones are constituted by calcilutite or calcarenite and interpreted as turbidites. They are evenly bedded in between the shales and dolostones, however, nodular limestones may be also found but less commonly. These strata may contain wrinkles and appear deformed, especially at the top of the Martin Point Member.

2.3 Biostratigraphy

The investigated interval studied comprises the uppermost Franconian to the Trempealeauan (Furongian, uppermost Cambrian). At the Martin Point section, the Tuckers Cove Member overlies strata with the trilobite *Hungia magnifica* (James and Stevens, 1986, in a personal communication with R. Ludvigsen, 1980), and boulders from the lower half of the unit carry a trilobite fauna that correlates with the North American Franconian Stage and Zone 5 of the Acado-Baltic Province (James and Stevens, 1986). However, in bedded strata, trilobites are scarce, especially in more distal facies (Barnes, 1988).

The conodont biozonation scheme (Fig. 2) of the Cow Head Group along the Cambrian-Ordovician boundary was widely described by Bagnoli et al. (1986), Barnes (1988), and James et al. (1989). Zhang and Barnes (2004) included in their study the Broom Point North section (lower proximal slope facies of the Tuckers Cove Member) and the Green Point section (distal slope facies of the Martin Point Member). The Tuckers Cove Member contains the *Eoconodontus notchpeakensis* zone in Broom Point North, while Martin Point Member has also the *C. proavus* and the *C. Caboti* zones, and part of the *C. Intermedius* zone in Green Point. This same interval, where FAD of *C. Intermedius* occurs at the Green Point GSSP, is correlated with the top (James and Stevens, 1986) of the Martin Point Member at the Martin Point section (Stouge et al., 2017). Thus, the investigated Martin Point section (Fig. 2) spans, from bottom to top, the upper part of the *Proconodontus posterocostatus* Zone, the *Proconodontus muelleri*, the *Eoconodontus notchpeakensis* (e.g., Lawson Cove and Sneakover Pass sections in Utah, USA), the *C. proavus*, and the *C. Caboti* conodont zones on the global and North American conodont biozonation scheme (James and Stevens, 1986; Barnes, 1988; Miller et al., 2011; Li et al., 2017). The base of the *Eoconodontus notchpeakensis* Zone is marked by the global Uppermost Cambrian HERB (Hellnmaria–Red Tops Boundary) $\delta^{13}C$ excursion (Li et al., 2017) that has been also documented in the Green Point (Cambrian-Ordovician GSSP; Miller et al., 2011) and Martin Point (Azmy 2019a) sections. However, the *Proconodontus posterocostatus* and *Proconodontus muelleri* zones have not been documented yet in the Martin Point section. The Cambrian Stage 10 spans almost from the *P. postercostatus* to *C. caboti* (at the Cambrian-Ordovician boundary) conodont zones (Fig. 2) and its base has been found to be marked by a negative $\delta^{13}C$ excursion (N1) on the C-isotope profile of the Wa'ergang section in China (Li et al., 2017). A correlated $\delta^{13}C$ excursion (NL1) has been also documented by the Martin Point C-isotope profile (Fig. 2; Azmy, 2019b).

The sequence of conodont zones can be correlated with trilobite zones *Saukia* (subzones *Rasettia magna, Saukiella junia, Saukiella serotina, Corbina apopsis*) and *Missisquoia* (subzones *Missisquoia depressa*) from the Upper Cambrian and lowest Ordovician found in the Wichita Mountains area (Barnes, 1988; Stitt, 1977; Fig. 2).

Radiolarian assemblages from the Tuckers Cove Member in Martin Point were described by Won and Iams (2002). This fauna is suggested to belong to the Franconian and includes *Subechidnina florea, Echidinina? Stevensi*, *Subechidnina pressa* y *Subechidnina gracilis*, *Echidnina irregularis*, and *Pararcheoentactinia reedae* group. Barnes (1988) reported *Dendrograptus* in the top of the Martin Point Member. However, it is the overlying Broom Point Member (lowermost Ordovician) that presents a greater abundance and variety of this kind of fossils.

Other groups of fossils have been discovered in western Newfoundland sections, such as acritarchs, chitinozoans, scolecodonts (Williams, 1997) and brachiopods (Barnes, 1988), still their stratigraphic resolution is yet to be evaluated (Cooper et al, 2001).

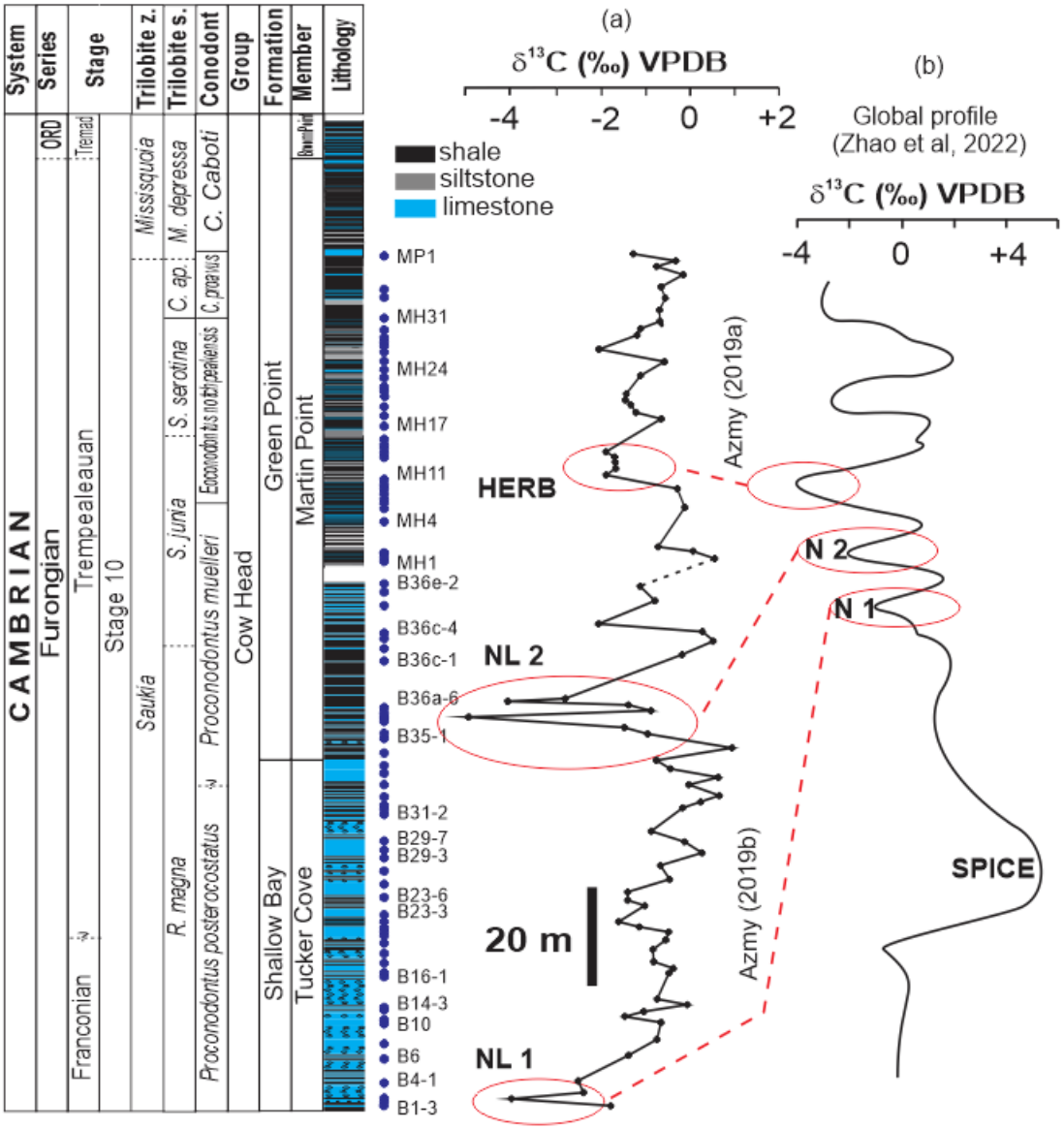

Fig. 2. Stratigraphic framework of the investigated carbonates in western Newfoundland, showing the $\delta^{13}C$ profiles, the main changes, bed number, positions of the samples, trilobite and conodont zonation scheme (Barnes, 1988; Li et al., 2017; Stitt, 1977) for (a) Post-SPICE (Azmy, 2019b) and HERB intervals (Azmy, 2019a; Wang and Azmy, 2020), and (b) C-isotope global correlation from Zhao et al. (2022).

Chapter III

Methodology

3.1 Sampling and Elemental Analysis

Samples (Appendix 1; Fig. 2) were collected from the most micritic lime mudstones interbeds at the Martin Point section (49° 40′ 51″ N, 57° 57′ 36″ W; Fig. 1; James and Stevens, 1986; Cooper at al., 2001), western Newfoundland, at high resolution with intervals as narrow as 30 cm (Fig. 2). Representative sample selection was guided by results from an earlier C-isotope stratigraphic study on the same succession (Azmy, 2019a, b). Thin sections of the micritic carbonates were stained with Alizarin Red-S and potassium ferricyanide solutions (Dickson, 1966) and examined petrographically using a polarizing microscope to locate the most micritic spots. Cathodoluminescence (CL) examinations were performed with a Technosyn 8200 MKII cold cathode instrument operated at 8 kV accelerating voltage and 0.7 mA current.

The mirror-image slab of each cut thin section was polished, cleaned with deionized water in an ultrasonic bath, and dried overnight at 40°C prior to sampling. Samples (200 mg) were extracted from the most micritic material of the cleaned slab.

For elemental analyses (Appendix 1), the sample powder was digested in 2.5 % (v/v) pure HNO_3 for 70–80 minutes and analyzed for major and trace elements using ICP-MS Neptune (Thermofisher Scientific) at Pôle de Spectrométrie Océan (PSO, Ifremer, Brest, France). The relative uncertainties of the measurements are better than 5% using BHV02 and internal standards. The calculations of major and trace element concentrations are based on an insoluble residue-free carbonates (100% soluble dolomite or calcite; Brand and Veizer, 1980) and the cerium anomaly (Ce/Ce*) was obtained with the following formula (Bau and

Dulski, 1996), using Post-Archean Australian Shale (PAAS) instead of shale normalized values (SN) for normalization:

$$(Ce/Ce^*)_{SN} = Ce_{SN} / (0.5\ La_{SN} + 0.5\ Pr_{SN})$$

3.2 Zn-isotope Analysis

For the zinc isotope analysis (Appendix 1), powder samples (between ~50–100 mg) were weighted, digested in HCl-HNO_3 and evaporated to dryness. Residues were dissolved in 5 mL 6N HCl and centrifuged to remove undissolved organic matter and keep as archive solutions. Zn isotopes were separated from the matrix using ion-exchange chromatography columns, following the procedure adopted by Maréchal et al. (1999), where 2 mL of macroporous AG MP-1 resin (100–200 mesh Biorad) was loaded on polypropylene columns. The resin was cleaned with 10 mL deionized water, 8 mL HNO_3, and again with 10 mL deionized water. Prior to sample loading, the resin was conditioned with 4 mL 6N HCl. An aliquot of the sample archive solution, containing 200–300 ng Zn, was loaded on the column in 6N HCl. The matrix was eluted in 2.5 mL 6N HCl, 10 mL 2N HCl, and 4 mL 0.24N HCl, and Zn was collected in 18 mL 0.012N HCl. The solution was evaporated to dryness on a hot plate at 90°C and the residue was dissolved in 2% HNO_3 for isotopic analyses.

Zinc isotopes were measured by MC-ICP-MS Neptune (Thermofisher Scientific) at Pôle de Spectrométrie Océan (PSO, Ifremer, Brest, France) in low-resolution mode using the Cu-doping method (Cu NIST SRM 3114) to correct for instrumental mass bias (Maréchal et al., 1999). A standard-sample-bracketing method was applied by measuring the isotopic standard Zn NIST SRM 683 doped with Cu NIST SRM 3114 before and after each sample. Zinc isotopes are reported in the conventional delta notation:

$$\delta^{66}Zn\ (‰) = [(^{66}Zn/^{64}Zn)_{sample}/(^{66}Zn/^{64}Zn)_{SRM683} - 1] \times 1000$$

However, for consistency with values reported in the literature, the Zn isotope composition is reported relative to the JMC-Lyon isotopic standard (Archer et al., 2017). The precision of analyses is reported as 2σ calculated based on replicate measurements of the standard Zn NIST SRM 683. External precision is determined using the USGS geostandard BHVO-2 for which three aliquots were processed on three different columns following the same procedure applied to samples. The total Zn in blank was <5 ng.

3.3 I/(Ca+Mg) Analysis

For I/(Ca+Mg) analysis (Appendix 1), the protocol followed was suggested by Hardisty et al. (2017). Powdered samples (~ 3 to 5 mg) were sonicated in 1 mL deionized water, centrifuged and decanted. Samples were digested in 3% HNO_3, sonicated for ~10 minutes and centrifuged. The supernatant was diluted with nitric acid and 0.25 % tetramethyleammonium hydroxide (TMAH) before running on an Agilent 8900 triple quad inductively coupled plasma mass spectrometer (ICPMS). Blanks, international (VWR AVS titrino IC 1000 mg/L), and internal standards were also prepared and treated similarly. Analytical uncertainties (monitored by Alfa Caesar's 0.1 N potassium iodate) were better than 5 %.

Chapter IV

Results

Petrographic examinations show that the investigated carbonates of the Martin Point section are mainly non-ferroan lime mudstones, with micritic (≤4 μm) to near-micritic (10 μm) grain size and they appear non-luminescent under the CL (Fig. 3). Minor organic matter might occur sporadically along stylolites and solution seams. Microfractures are rare and filled with carbonate cements.

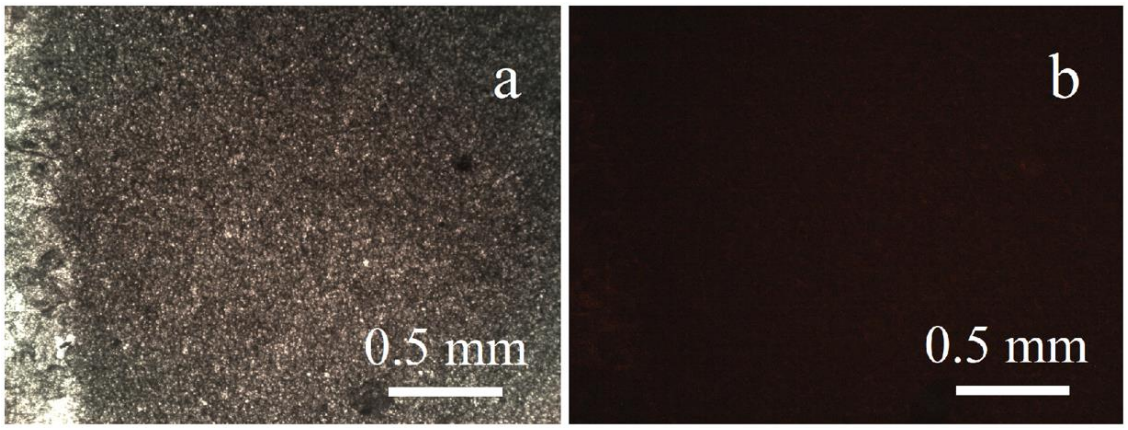

Fig. 3. Photomicrographs of the studied carbonates displaying (a) micritic to near-micritic lime mudstones with a post-diagenetic carbonate vein to the left (crossed polars; sample B4-1) and (b) CL image of (a).

The investigated section spans the Upper Cambrian and the C-isotope stratigraphy (Fig. 2) records two post-SPICE (Steptoean Positive Isotope Excursion) negative excursions (NL1 and NL2; Azmy, 2019b) and the overlying HERB (Hellnmaria – Red Tops Boundary) negative excursion (Azmy, 2019a, Wang and Azmy, 2020). The paleoenvironmental proxies of the HERB event (upper Martin Point section) have been studied by Wang and Azmy (2020) and the current study investigates the variations in the δ^{66}Zn and I/Ca+Mg) across

both of the post-SPICE and HERB events including the paleoenvironmental proxies of the post-SPICE carbonates (lower section of Martin Point).

Table 1. Summary statistics of isotopic and elemental geochemistry of the investigated post-SPICE and HERB carbonates in the Martin Point section. The highlighted values are from Wang and Azmy (2020).

	$\delta^{13}C_{carb}$ (‰ VPDB)	TOC (%)	$\delta^{66}Zn$ (‰ JMC Lyon)	I/(Ca+Mg) µmol/mol	Zn (ppm)	Sr (ppm)	P (ppm)	Ni (ppm)	Cu (ppm)	Mn (ppm)	Fe (ppm)	Al (ppm)	∑REE (ppm)	V (ppm)	Mo (ppm)	U (ppm)	Th/U	Ce/Ce*	Mn/Al	Fe/Al	Al/Ti
HERB																					
n	48	36	18	11	11	17	17	17	17	17	17	17	17	17	17	17	17	17	17	17	17
Mean	-0.61	1.02	0.33	0.13	6.2	356	142	4.1	7.6	380	2542	356	49	4.9	2.5	1.1	1.37	0.85	0.35	1.7	38.4
STDV	0.80	0.62	0.11	0.09	7.8	226	45	1.9	3.1	142	1876	226	23	1.5	2.6	0.9	1.57	0.07	0.20	0.9	13.3
MAX	+1.00	3.10	+0.48	0.31	21.7	980	252	8.5	17	572	6900	980	95	7.8	11.7	3.6	5.05	0.96	0.93	4.5	79.6
MIN	-2.05	0.30	+0.09	0.02	0.6	165	85	1.9	4.7	150	785	165	25	2.2	0.8	0.2	0.12	0.70	0.11	1.1	19.3
post-SPICE (NL1 & NL2)																					
n	47	26	29	19	30	30	30	30	30	30	30	30	30	30	30	30	30	30	30	30	30
Mean	-0.92	0.70	+0.33	0.18	7.9	317	214	6.6	4.3	395	9975	3662	76	11.1	0.63	1.07	1.76	0.92	0.06	3.1	61
STDV	1.18	0.66	0.13	0.13	8.6	178	128	6.9	3.9	295	10997	2473	35	8.7	1.07	0.79	1.22	0.06	0.04	2.5	33
MAX	+0.96	2.98	+0.73	0.48	40.9	992	573	35.8	19.8	1176	56094	11229	155	39.4	4.79	3.21	5.28	1.04	0.17	11.3	146
MIN	-4.79	0.10	+0.12	0.02	0.7	121	45	0.7	0.5	125	1212	456	18	1.7	0.04	0.12	0.22	0.79	0.01	0.8	23

The chemical attributes of the investigated carbonates are tabulated in Appendix 1 and Table 1 summarizes their statistics. The mean values of the investigated paleoenvironmental proxies of the post-SPICE and HERB events are generally comparable (Fig. 4). The mean $\delta^{66}Zn$ values in both intervals are almost identical (+0.3 ± 0.1 ‰ JMC-Lyon; Fig. 4; Table 1) and similar to average continental crust ($\delta^{66}Zn$ = +0.31 ± 0.11‰; Little et al., 2014). Similarly, those of I/(Ca+Mg) are very comparable (0.1 and 0.2 µmol/mol, respectively) and less than the lower boundary value established for oxic conditions (2.5 µmol/mol, Lu et al., 2016). Although the post-SPICE carbonates (spanning NL1 and NL2) have slightly higher mean values of P, ∑REE, and Th/U, they are significantly enriched in Al and Fe than their HERB counterparts (Fig. 4; Table 1). However, the rest of the proxies (Zn, Cu, Ni, Ce/Ce*, and Mn) are almost comparable (Fig. 4).

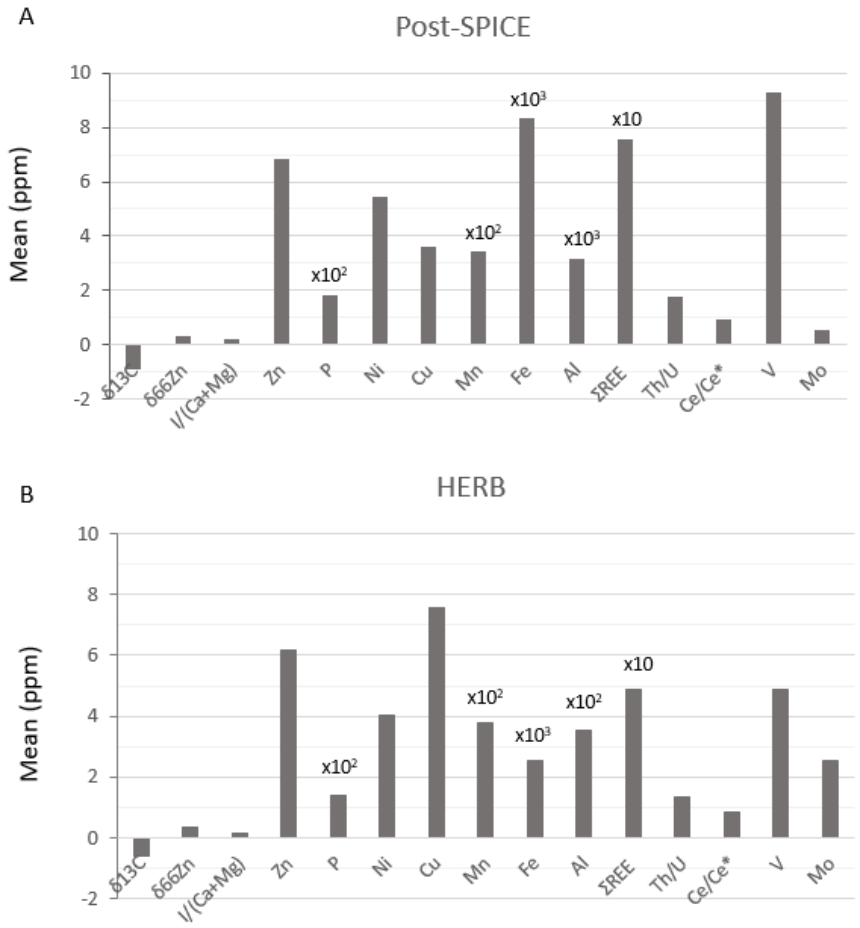

Fig. 4. Bar charts showing the mean values for $\delta^{13}C$, $\delta^{66}Zn$, I/(Ca+Mg) and trace elements of the (a) Post-SPICE and (b) HERB events in the investigated Martin Point carbonates.

The Sr values (post-SPICE 290 ± 184 ppm vs. HERB 356 ± 226 ppm; Table 1; Fig. 5) are comparable in the post-SPICE and HERB carbonates. They exhibit insignificant correlations (R^2 <0.02–0.18) with their Zn, P, Ni, Cu, Fe, Th/U, ∑REE, Al, Mn, Fe, $\delta^{66}Zn$, and I/(Ca+Mg) counterparts and even when the R^2 is considerable, the correlation has an opposite trend to that expected from diagenetic alterations (Fig. 5o).

Sample B32 shows the highest Mg content (absolute values) and lowest [Sr], which suggests possible influence of diagenesis on the $\delta^{66}Zn$ (highest value), although the values of

other paleoproxies (e.g., total REE, Mn, Fe, Al, Zn) still fall within the range of the rest of the samples. Therefore, its $\delta^{66}Zn$ should be taken with caution.

The profiles, reconstructed from the enrichment factor (EF) of the elemental proxy values, exhibit minor variations correlated with NL1 but more pronounced shifts with NL2 of the post-SPICE interval (Fig. 6). On the other hand, most of these profiles show noticeable variations correlated with the HERB event (Fig. 6).

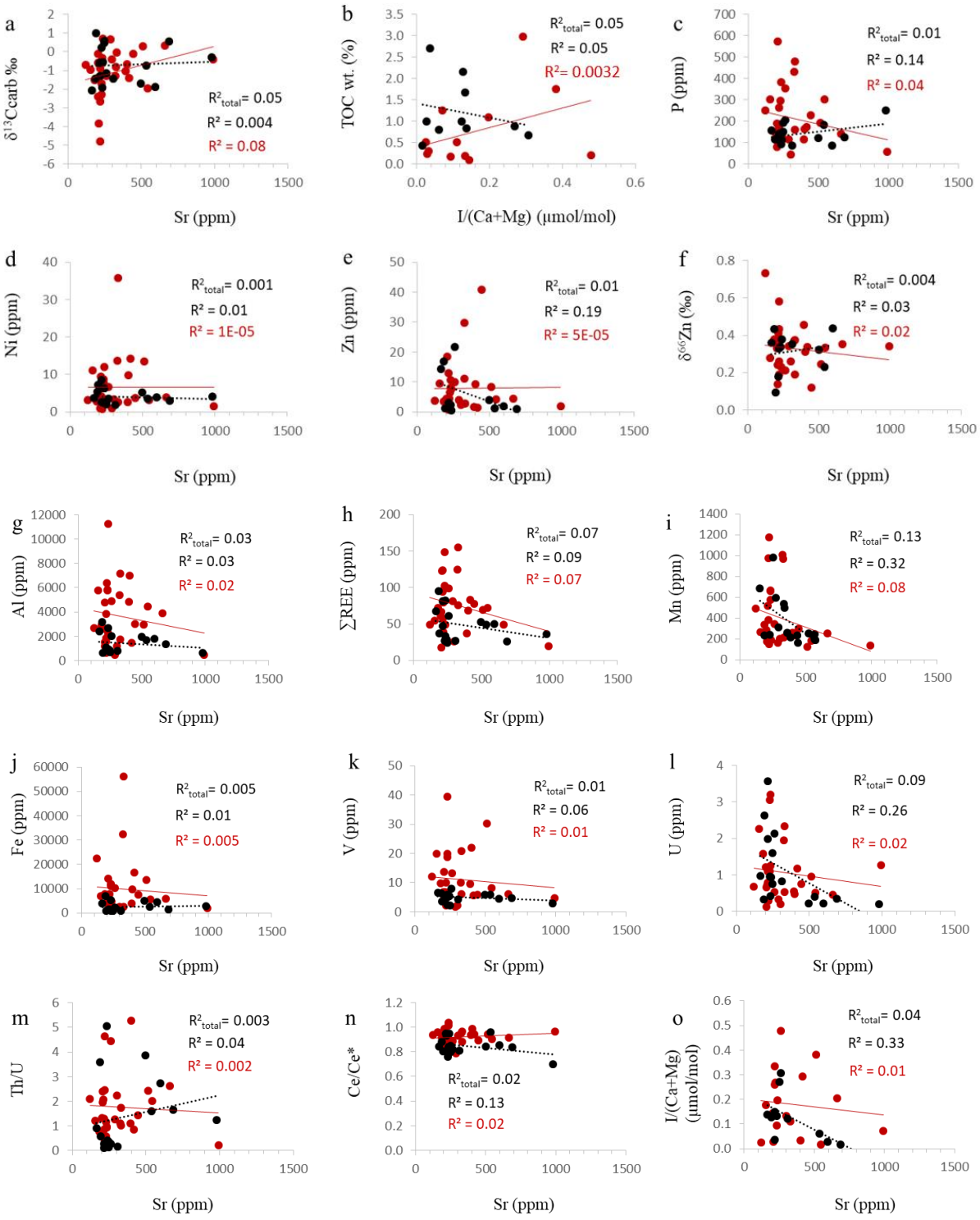

Fig. 5. Scatter diagrams showing the correlation of Sr with (a) $\delta^{13}C$, (c) P, (d) Ni, (e) Zn, (f) $\delta^{66}Zn$, (g) Al, (h) ∑REE, (i) Mn, (j) Fe, (k) V, (l) U, (m) Th/U, (n) Ce/Ce*, (o) I/(Ca+Mg) and (b) TOC with I/(Ca+Mg) for the post-SPICE (red dots) and HERB (black dots) carbonates in the Martin Point section.

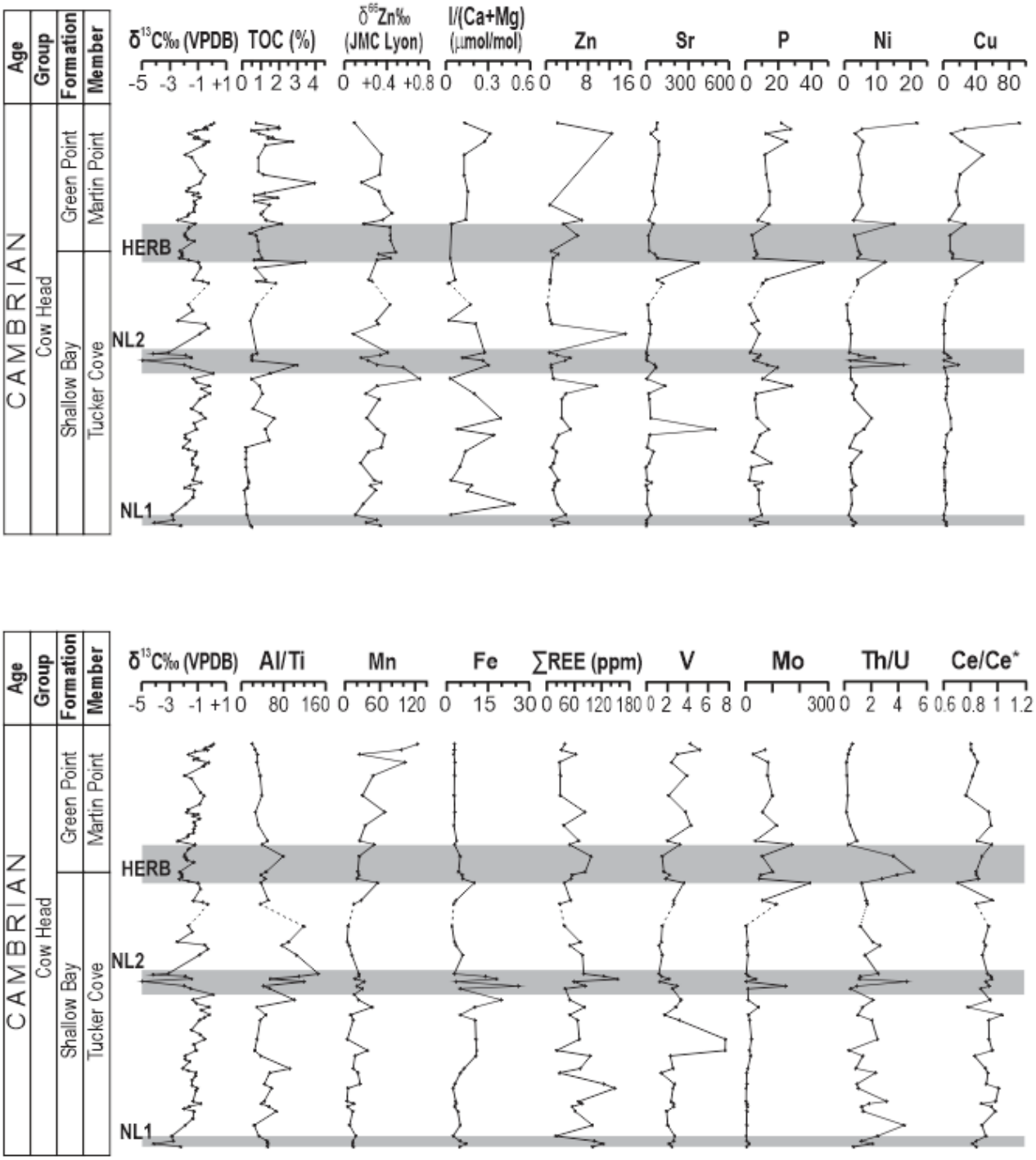

Fig. 6. Profiles of TOC, δ^{66}Zn, I/(Ca+Mg), Zn, Sr, P, Ni, Cu, Al/Ti, Mn, Fe, ∑REE, V, Mo, Th/U and Ce/Ce* for post-SPICE and HERB. The δ^{13}C profile is reproduced from Azmy (2019a, b). The TOC data of HERB are derived from Wang and Azmy (2020) and post-SPICE from Okafor (2023).

Chapter V

Discussion

5.1 Evaluation of diagenetic impact

5.1.1 Petrographic Preservation

The petrographic preservation of the Martin Point carbonates is only summarized here since it has been already discussed in detail by Azmy (2019a and b) and Wang and Azmy (2020). Petrographic examinations of the studied carbonates indicate that they are mainly fabric-retentive lime mudstones with minimum recrystallization. They have micritic (<4 μm) to near-micritic (10 μm) grain size (Fig. 3a) and exhibit dull to non-luminescence (Fig. 3b) under cathodoluminoscope (CL), which suggest low water/rock interaction ratios and a high degree of petrographic preservation. Luminescence in carbonates is controlled by trace element contents (Machel and Burton, 1991; Machel, 2000), of which Mn^{2+} and Fe^{2+} are the most important cations substituting Ca^{2+} in the crystal lattice (Leverenz, 1950) and acting as activator and quencher, respectively.

However, the CL technique is only complementary, for it has been demonstrated that cation exchange can occur without significant visible change in the crystal size and fracture-filling cements of deep-burial settings may have high Fe and appear dull under CL (Rush and Chafetz, 1990). Therefore, petrographic examination alone cannot confirm sample preservation but has to be combined with other tools. Yet, if redistribution of mass takes place within length scales over which the system is fundamentally closed and this length scale is smaller than sampling, a fairly faithful signal can be recovered (Fantle et al., 2020).

5.1.2 Geochemical preservation

Progressive burial of sediments is associated with an increase in temperature with depth and the reaction of sediments with the diagenetic fluids, which results in the depletion of some elements such as Sr and enrichment of others such as Mn, Fe, Al, and ∑REE (Veizer, 1983; Azmy et al., 2011; Wang and Azmy, 2020). However, diagenesis might not significantly alter the contents of other elements (such as Ni, P, Zn, Th, U, Ce/Ce*, δ^{66}Zn, and I/(Ca+Mg)), which are reliable environmental proxies (Veizer, 1983; Śliwiński et al., 2010; Pattan et al., 2013; Acharya et al., 2015; Yan et al., 2019; Wörndle et al., 2019).

The Sr values of the Martin Point carbonates show insignificant ($R^2 \leq 0.1$) correlations (Fig. 5) with their δ^{13}C, TOC, P, Ni, Zn, δ^{66}Zn, Al, ∑REE, Mn, Fe, V, U, Th/U, Ce/Ce*, and I/(Ca+Mg) counterparts, which is also evident from the Sr profile (Fig. 6). This is consistent with the petrographic preservation (Azmy 2019a and b; Wang and Azmy, 2020) and also supports the preservation of at least near-primary signatures of the environmental proxies. The deposition of the investigated Martin Point lime mudstones in dysoxic settings (James and Stevens, 1986; Landing, 2012; Azmy, 2019a and b; Wang et al., 2020) likely contributed to the relatively higher Mn and Fe contents (Fig. 5; Table 1) than their modern counterparts (Morrison and Brand, 1986).

Although Sr values may exhibit apparent moderate correlation ($R^2 = 0.3$) with the HERB I/(Ca+Mg), the correlation is negative and opposite to the diagenetic trend and thus supports at least near-primary I/(Ca+Mg) values (Fig. 5o; Veizer, 1983; Derry et al., 1992).

The Mg/Ca ratios have insignificant correlations with their δ^{66}Zn and I/(Ca+Mg) counterparts ($R^2 = 0.0009$ and 0.02, respectively; Appendix 1). Iodine is incorporated into the calcite crystal as $[IO3]^-$ and not $[I]^-$ (Lu et al., 2010) and minor alteration or dolomitization of carbonates, particularly when earlier and not associated with significant increase in crystal size, is therefore unlikely to influence their I contents. A recent study by Lu et al. (2021)

documented no significant difference in the I/(Ca+Mg) signatures of recrystallized and non-recrystallized samples.

In summary, the petrographic and geochemical criteria of the investigated lime mudstones support the retention of at least near-primary geochemical signatures that reflect variations in the paleoenvironment during deposition.

5.2 Paleoenvironmental proxies

In contrast to siliciclastic rocks, carbonate rocks precipitate directly from seawater recording its geochemistry. The relative fluctuations of sea level lead to variations in water chemistry, and therefore, in carbonates, whose geochemical signatures are sensitive recorders of changes in environmental conditions, and have been used as proxies to track many parameters (e.g., Meyer et al., 2012). In this study, Zn-isotope compositions and I/(Ca+Mg) ratio proxies are analyzed along trace elements in correlation with the $\delta^{13}C$ curve where the Late Cambrian events NL1, NL2, and HERB have been recognized in western Newfoundland (eastern Laurentia; Azmy, 2019a, b).

5.2.1 Zn isotope

Zinc is a bio-limiting micronutrient (Morel et al., 1994) that follows a vertical distribution in the ocean. It is depleted from the marine surface water by biological pumping and re-precipitated and enriched in deeper water (Bruland, 1980). Zn sequestration takes place through its incorporation in organic matter, involving minimal or no isotopic fractionation (Zhao et al., 2014), and through metabolic uptake into the cells of, mainly, phytoplankton. Isotopic fractionation occurs as light Zn (^{64}Zn) is preferentially assimilated

and removed by these microorganisms. On the other hand, regeneration of Zn in deep waters is produced by bacterial activity which oxidizes organic matter and by the dissolution of sinking particles (Morel et al., 1994).

Shiller and Boyle (1985) suggested an oceanic residence time of ~ 50,000 years for zinc, considering riverine sources as the most important input to seawater. Zinc is present in seawater in the form of hydroxide and carbonate complexes (Millero, 1996) and is incorporated in carbonate minerals in trace amounts, both as tetrahedral complexes on the calcite surface and substituting Ca^{2+} in the crystal lattice (Reeder et al., 1999). It appears to be an ideal substitution for Ca^{2+}, since it is strongly enriched in the solid during co-precipitation with calcite (Reeder et al., 1999). Hydroxide and carbonate complexes have not shown significant fractionation in aqueous solutions (e.g., Maréchal and Sheppard, 2002) and the isotopic composition of the carbonate fraction has been assumed to record the one of the seawater in which the carbonates formed (e.g., Pichat et al., 2003).

While deep ocean isotopic Zn is relatively homogeneous worldwide (+0.5 ‰; Bermin et al., 2006), surface water values are variable (-1.1 to +0.9 ‰) and have been attributed mainly to the uptake of the lighter isotopes by primary producers (John and Conway, 2014). Consequently, heavy isotopes are incorporated in carbonate minerals, recording higher $\delta^{66}Zn$ values. Due to the great influence of phytoplankton in the variability of $\delta^{66}Zn$ values in seawater, the Zn isotopic composition of bulk carbonate sediments has been successfully used to track fluctuations in primary productivity (e.g., Kunzmann et al., 2013; Wang et al., 2018).

Another factor to be taken into consideration is weathering input. Crustal $\delta^{66}Zn$ and silicate weathering runoff have low values in the range between +0.1 and +0.3 ‰ (Maréchal

et al., 2000; Chapman et al., 2006), while carbonate weathering is generally a supply of ^{66}Zn (Chen et al., 2008).

The isotopic Zn profile in the present section shows values that range from +0.09 to +0.73 ‰ (Table 1; Fig. 6) and varies consistently along the pertinent events. Although, the high end member $\delta^{66}Zn$ value (+0.73 ‰) of sample B32 is associated with the lowest Sr and highest Mg contents (Fig. 2, Appendix 1; Table 1), its other geochemical proxy signatures fall within the same range of the rest of lime mudstone (calcite) samples and no correlation has been found between the $\delta^{66}Zn$ and Ca/Mg values ($R^2 = 0.0009$). This is consistent with earlier studies, which suggested that dolomites may still retain at least their near-primary $\delta^{66}Zn$ signatures (e.g., Kunzman et al., 2013; John et al., 2017; Yan et al., 2019). The profile shows localized increments at the base of the NL1, NL2, and HERB (up to +0.37 ‰, +0.73 ‰, and +0.48 ‰ (JMC-Lyon), respectively; Fig. 6), following then a general decrease upwards. Different scenarios are proposed for this tendency: a) the depletion of ^{64}Zn by biological uptake due to primary productivity and its posterior inhibition, which caused a progressive drop in the $\delta^{66}Zn$ values, b) preferential weathering of ^{66}Zn-enriched biogenic carbonate over ^{64}Zn-enriched silicates, and posterior inversion of the situation due to unavailability of carbonate, or c) a combination of these factors. The scenarios are explored below.

5.2.1.1 Primary productivity

In the literature, values resulting from a depletion in ^{64}Zn due to a bloom of bioproductivity are in the range between ~+0.6 and +1.1 ‰ (e.g., Kunzmann et al., 2013) or more (~+0.7 to +1.3 ‰, Pichat et al., 2003; shifts from ~+0.2 to +1.1 ‰, Chen et al., 2021). These are higher than the values or the rate of the increments in this study, which do not show such significant change. Thus, the isotopic Zn signature in these carbonates could be

revealing only a certain extent of primary productivity, as the magnitude of the positive peaks does not account for significant biological uptake.

The profiles of the elements Zn, P, Ni, and Cu (Fig. 6) do not display parallel behaviour with respect to the δ^{66}Zn signature. These are considered to be strong bioproductivity proxies (Brumsack, 2006; Chen et al., 2017; Shimura et al., 2014; Śliwiński et al., 2010), as they constitute essential components in the biological cycle of marine life and their concentration in the seawater column follows a characteristic nutrient-like distribution: they are depleted at the surface and show an increment towards the deep ocean (Bruland, 1980). Their distribution in the ocean is linked to assimilation by marine organisms, release into dissolved nutrients in surface waters by different biological processes and into deeper water by sinking particles of decomposing organic matter and, furthermore, to the slow mixing between these two water masses (Tyrell, 1999). Thus, parallel behaviour of the Zn, P, Ni, and Cu concentrations with the δ^{66}Zn profile (Fig. 6) could indicate that the isotopic signature is considerably affected by the activity or lack of activity of organisms such as phytoplankton. These trace elements' profiles along the events do not support a major bloom in bioproductivity and are consistent with the relatively low δ^{66}Zn magnitudes.

Similarly, the TOC profile, which has been utilized as the most direct proxy for primary productivity (Schoepfer et al., 2015), does not suggest especially high organic activity throughout the section (Fig. 6; Okafor, 2023). The values are overall low, with means of 0.60 % (± 0.66 %) and 1.02 % (± 0.62 %) for the post-SPICE and HERB samples, respectively (Table 1). In comparison, TOC data from carbonate rocks deposited during the late Devonian Frasnian-Famennian biotic crisis plotted by Wang et al. (2018) based on Chen et al. (2005), yielded a mean of 0.13 %); Rühlemann et al. (1996) obtained TOC < 0.4 % for Late Quaternary minor productivity settings; lastly, high productivity TOC values from Ediacaran-period dolostones range from 0.01 to 4.84 % (Gao et al., 2020). Therefore, the

relatively low TOC of the Martin Point carbonates might point to only a certain degree of bioproductivity, which agrees with the modest δ^{66}Zn increments.

On the contrary, bioproductivity proxies along the studied events seem to show variations opposite to the isotopic Zn profile, as increments in Zn, P, Ni, Cu, and TOC coincide with drops in the δ^{66}Zn values (Fig. 6). These trace elements are strongly complexed by organic matter and could be suggesting an increase in anoxic sedimentation (e.g., Acharya et al., 2015). Relatively more reducing settings agree with the progressive inhibition of primary producers and consequent decrease in the δ^{66}Zn values, while dysoxic waters could aid only minor bioproductivity and, therefore, certain depletion of the seawater ^{64}Zn, resulting in modest positive shifts in the δ^{66}Zn profile and consistent with the δ^{66}Zn values of the carbonates herein.

Comparable δ^{66}Zn values to the ones in this study have been reported for carbonates in dysoxic conditions (~0 to +0.8 ‰, Cretaceous Oceanic Anoxic Event 2, Chen et al., 2021) and deep corals assumed to record the δ^{66}Zn values of the ambient seawater (~0 to +0.6 ‰, Little et al., 2021). Indeed, the Martin Point carbonates were interpreted to be deposited mainly under dysoxic conditions (Azmy, 2019b), which would not favour a major bloom in bioproductivity. Indicators of redox changes in seawater support a generally dysoxic setting as well, as evaluated below.

Manganese and iron's enrichment factors reflect variations in redox conditions (Fig. 6), since they represent the fraction of the elements which are not derived from terrigenous influxes (Acharya et al., 2015), allowing to evaluate their enrichment relative to average crustal abundance (Tribovillard et al., 2012). Relatively abundant concentrations of Mn and Fe in the water column would indicate more reducing conditions, as they become more soluble with less oxygenation (Middelburg et al., 1988). The opposite absence of significant

metal enrichment has been interpreted as sediments deposited within substantially oxygenated bottom waters (Acharya et al., 2015). Generally, in the present profiles (Fig. 6), Mn and Fe enrichments coincide with negative $\delta^{66}Zn$ excursions, suggesting inhibition of bioproductivity by a relatively reducing water column. Similarly, the lack of Mn and Fe enrichment accompanying positive $\delta^{66}Zn$ shifts indicates a degree of relative oxygenation consistent with minor biological uptake of ^{64}Zn.

Vanadium enrichment has been associated with deposition under anoxic environments (Brumsack and Gieskes, 1983; Emerson and Huested, 1991) and it is, therefore, expected to be relatively more abundant in deep water sediments (Acharya et al., 2015). Its burial in these conditions is bound to organic matter (Breit and Wanty, 1991; Hetzel et al., 2009). Molybdenum commonly shows strong co-variation with vanadium and is generally enriched in anoxic sediments as well, making it a useful indicator of variations in paleoredox conditions (e.g., Anbar et al., 2007). It is removed from the solution to the sediments by adsorption to organic matter or by Fe-Mn oxy-hydroxides (Algeo and Maynard, 2004). The trend of these trace elements along the events is similar to the Mn and Fe counterparts (Fig. 6), endorsing the relation of redox settings to changes in the bioproductivity reflected in the $\delta^{66}Zn$ profile.

The described scenario supports a rise in sea level with minor drops during its main course. Regarding the HERB event, this is consistent with Miller et al. (2011), who have identified the *Eoconodontus notchpeakensis* zone as part of a low system track (LST) where a transgression was occurring. The sea-level rises probably caused the shoaling of more anoxic waters (Gill et al., 2011; Li et al., 2020), producing the emplacement of organic matter with elements such as P, Ni, or Cu (Gao et al., 2016), and an increment in anoxic sedimentation, as suggested by redox proxies. The deep-water mass likely mixed with relatively more oxygenated shallow waters and inhibited primary productivity, which is reflected in the

negative δ^{66}Zn excursions. Meanwhile, minor drops let primary producers thrive to some extent under more oxygenated water columns, shifting isotopic Zn compositions to slightly higher values as the organisms satisfied metabolic needs (e.g., Kunzmann et al., 2013) and, probably also, at the expense of nutrients previously delivered to the system by shoaling. Oxidation of organic matter could have made the nutrients available for biological uptake (Canfield, 1993, 1994; Böning et al., 2009).

Miller et al. (2003) identified full LST to highstand system tract (HST) cycles within each of the *Proconodontus posterocostatus* and the *Proconodontus muelleri* zones, which include the recognized NL1 and NL2, respectively, and the geochemical signatures of said events are comparable to those of the HERB event (Fig. 6). Therefore, a transgression with minor drops in the sea level took place during each of the NL1 and NL2 events as well.

5.2.1.2. Weathering inputs

Inputs of weathered biogenic carbonate provide an isotopic heavy source of Zn (~ +1.07‰) and drive oceanic δ^{66}Zn to higher values. Even if the contribution would be minor due to the low concentration of Zn in carbonates (Kunzmann et al., 2003), the addition of carbonate to the system could represent a fraction of the increasing isotopic Zn signature at the base of the events (Fig. 6). Preferential weathering of carbonate over silicate is probable, as carbonates are more easily weathered and dissolved in humid weather than silicates.

The slight increase in bioproductivity appears to have been favoured by a change in the oxygenation conditions associated with a minor drop in the sea level during non-major fluctuations. Therefore, it is possible that a drop in sea level led to the exposure of platform carbonates, making them available for weathering and susceptible to meteoric waters. While negative variations in the sea level are usually related to climate cooling, which diminishes the rate of chemical weathering, carbonates are still more prone to weathering than silicates

due to the difference in the temperature sensitivity of the dissolution rate (Wang et al., 2018; Palandri and Kharaka, 2004). Therefore, the carbonate source likely accounts for the weak positive shifts in the Zn isotopic signature together with primary productivity.

Weathering inputs of crustal material are considered a source of light isotopic Zn (Maréchal et al., 2000; Chapman et al., 2006) and could have driven seawater to relatively lower δ^{66}Zn values along the events (Fig. 6). In order to discern this, proxies of terrigenous inputs are assessed as follows.

REE, Al, and Ti are water-insoluble elements and are trapped in the carbonates as impurities. They mainly originate from continental weathering and can be monitors of the terrigenous influence in carbonates (e.g., Han et al., 2022; Zhao and Zheng, 2014). Al concentration is practically independent of the rock type, whereas Ti is mostly hosted in heavy minerals in sediments and sedimentary rocks (Spears and Kanaris-Sotiriou, 1976). The Ti fraction of sediment has been associated with detrital material (Wei et al., 2003), and Ti abundance is assumed to represent aeolian inputs in marine sediments. Low Al/Ti ratios have been related to glacial periods and vice versa (e.g., Yarincik et al., 2000; Wei et al., 2003; Bunzel et al., 2017).

The Al/Ti ratio displays positive shifts along the three events (NL1, NL2, and HERB; Fig. 6), with subpeaks within NL2 and NL1, suggesting consistent warm climate and a subsequent transgression of reducing waters which led to the inhibition of bioproductivity. The overall lack of aeolian input seems to be due to humid conditions. Instead, the subpeaks in the ratio, i.e. the low Al/Ti values in the events, and tentatively in between the events, support the occurrence of minor sea-level falls within the main transgression.

Wind-blown material (Gao et al, 1992; Nakai et al., 1993) during minor drops in sea level would deliver crustal isotopic Zn values to the ocean, however, the carbonate δ^{66}Zn

signature does not co-vary clearly with the negative shifts in the Al/Ti ratio. Therefore, and considering that a sea level rise was the leading process during each event, it is suggested that biological activity was a slightly enhanced phenomenon rather than wind-blown weathering regarding their influence in the isotopic Zn signature.

The ∑REE profile shifts show co-variation with different proxies for the HERB event and the NL2 (Fig. 6), implying that the main REE source was different. During the HERB and NL1, Al/Ti and ∑REE shift positively, attesting minor terrigenous input, which could represent contributions from riverine discharge, as it is the main source of REE in modern oceans, apart from atmospheric dust (Holser, 1997). Warm climate during the transgression is compatible with runoff, thus, riverine crustal material may have affected the isotopic Zn signature to an extent.

On the other hand, during the NL2 event, the ∑REE profile behaves similarly to redox proxies such as Fe and Mo, and also to the ones commonly coupled to organic matter, like Ni and P (Fig. 6). In fact, REE have been found to be complexed by organic matter too, and removed from solution by adsorption to the organic particles (e.g., Smrzka et al., 2019; Tang and Johanneson, 2003). This further supports the shoaling of more reducing waters which caused an increase in anoxic sedimentation and the consequent inhibition of primary productivity reflected in the decreasing tendency of the δ^{66}Zn profile. Riverine runoff does not seem to explain the isotopic Zn signature in this case.

In summary, the Zn-isotope profile exhibits variations correlated with the studied events (NL1, NL2, and HERB), which are consistent with a transgression scenario and warm climate that involved:

- The spread of deep, more reducing water masses with episodes of shoaling, causing the inhibition of bioproductivity, which was the most important factor in the negative shifts of the $\delta^{66}Zn$ signature.
- Riverine runoff, which slightly contributed to the decreasing isotopic Zn compositions during NL1 and HERB but was not significant for NL2.
- Minor drops in the sea level during the main course of the transgression that resulted in:
    - Slight blooms in bioproductivity, favoured by the relative oxygenation of the water column.
    - Exposure of silicate and carbonate rocks, whose weathering was limited due to the relatively low temperature and among which carbonate rocks were more susceptible and significant to the $\delta^{66}Zn$ signature.

5.2.2 I/(Ca+Mg) ratio

In modern oceans, iodine concentration is fairly uniform (0.45 µmol/l; Elderfield and Truesdale, 1980) and principally controlled by the burial of organic carbon in marine sediments (Muramatsu and Wedepohl, 1998). The iodine cycle through seawater and sediments seems to be biologically and photochemically mediated (Spokes and Liss, 1996; Wong et al., 2018). Its budget in the ocean is not meaningfully affected by riverine input, carbonate precipitation/dissolution, or hydrothermal fluxes (Lu et al., 2010). Furthermore, iodine primary signatures are influenced by local redox conditions more than large-scale changes (Zhou et al., 2015).

Iodine is highly affected by redox conditions and present dissolved in solution as iodide (I^-) in more reducing settings, or as iodate (IO_3^-) in oxygenated conditions, as these

two are its most thermodynamically stable forms (Wong and Brewer, 1977). Although both anions are monovalent, they have shown different behaviours in sorption processes (e.g. Hu et al., 2005). Carbonate minerals only incorporate the oxidized species during precipitation, since IO_3^- appears to be an appropriate substitution for CO_3^{2-} in the crystal lattice (Podder et al., 2017). Therefore, their I/(Ca+Mg) content seems to be proportional to the iodate concentration of the solution (Lu et al., 2010), such as carbonates formed in the vicinity of waters depleted in oxygen, record lower ratio values (Lu et al., 2017). This, plus iodine's seawater residence time of ~300,000 years (Broecker and Peng, 1982), allows the I/(Ca+Mg) ratio to behave as an indicator of redox variations in the seawater from which the carbonates precipitated (e.g., Wei et al., 2019). Lu et al. (2016) proposed a threshold of 2.5 µmol/mol, by which lower values indicate the presence of oxygen-depleted water.

The Martin Point carbonate I/(Ca+Mg) ratios record low values that range from 0.02 to 0.48 for the investigated section (Table 1, Fig. 6) and suggest locally reduced water columns. Similar low I/(Ca+Mg) ratios have been reported in Palaeozoic carbonate successions recording expansion of anoxia such as bulk carbonates from Lower Ordovician and also Silurian Laurentia that yielded ratios within the range of 0 and 0.5 µmol/mol (Edwards et al., 2018; Young et al., 2019). Modern I/(Ca+Mg) concentrations in sea surface waters above Oxygen Minimum Zones (Rue et al., 1997), which represent current low oxygen settings, vary between 0 and 2.5 µmol/mol in contrast to values around 5 µmol/mol for well-oxygenated conditions (Lu et al., 2016).

Instead, the Great Oxygenation Event of the Precambrian documented values near 2 µmol/mol (e.g., Hardisty et al., 2014), reasonably far from the ratios of the present study and it is noteworthy that the Proterozoic was an eon with relatively low oxygen. The magnitude of the peaks in the Martin Point samples is similar to previous studies which indicate local redox shifts within conditions of low overall I/(Ca+Mg) ratios (e.g., Bowman et al., 2021).

Therefore, the values are consistent with past interpretations on the slope environment's dysoxic conditions (Azmy, 2019b) and support not only a relatively reducing water column product of a general rise in the sea level for each of the studied events, but also the consequent inhibition of primary productivity as interpreted by the isotopic Zn profile. This is reinforced by other proxies as elaborated below.

The normalization of Mn and Fe to Al has been shown to decrease the influence of the source mineralogy (Poulton and Raiswell, 2005), standardizing the proxies in order to apply them to different sediment types (Clarkson et al., 2014). Mn/Al ratios in the current study (0.06 ± 0.04 post-SPICE; 0.35 ± 0.20 HERB; Table 1) are relatively enriched with respect to upper continental crust values (0.0075; McLennan, 2001). Similarly, Fe/Al yielded higher concentrations (3.1 ± 2.5 post-SPICE; 1.7 ± 0.9 HERB; Table 1) in comparison to the crustal average (0.44; McLennan, 2001). Since enrichments in Mn and Fe are associated with more reducing conditions, these values support the interpretation based on the I/(Ca+Mg) ratios.

Vanadium and molybdenum commonly show strong co-variation and their enrichment has been associated with relatively reducing conditions (Acharya et al., 2015; Anbar et al., 2007). Vanadium upper crust values of 60 ppm (McLennan, 2001) are higher than those of the present study (11.1 ± 8.7 ppm post-SPICE; 4.9 ± 1.5 ppm HERB; Table 1; Fig. 6), probably due to the dysoxic character of the slope environment (Azmy, 2019b). However, Dolenec et al. (2001) also reported carbonate V concentrations (2–48 ppm) lower than 60 ppm for a period of LST recognized in a Permian-Triassic boundary section. Molybdenum values for the post-SPICE and HERB events in the Martin Point carbonates (0.63 ± 1.07 ppm and 2.5 ± 2.6 ppm, respectively) are also comparable to those of Dolenec et al. (2001) (<6 ppm). Additionally, the positive shifts during the NL2 and at the base and top of the HERB event in the Martin Point samples show high enrichment in comparison with typical concentrations for marine carbonates, such as Carboniferous samples of Voegelin et

al., 2009 (<1 ppm), and continental crust values (1.5 ppm; McLennan, 2001). Therefore, the present V and Mo concentrations are consistent with the relatively reducing conditions suggested by the I/(Ca+Mg) ratio.

Manganese, iron, vanadium, and molybdenum likely increased above average concentrations for carbonates due to the influx of deep waters and especially the shoaling with the transgressions during the NL1, NL2 and HERB events.

Thorium (Th^{4+}) is mainly produced from clays formed by continental weathering and is unaffected by redox changes in the water column. In contrast, U is scavenged in anoxic sediments, causing a rise in the Th/U of the water. Therefore, a low Th/U ratio could mean a relative enrichment of U in seawater, according to the interpretation by Wignall and Twitchett (1996). Throughout the studied events, the ratio behaves generally opposite to elements that are complexed by organic matter (e.g., P, V; Fig. 6), reinforcing this classic interpretation, since U is commonly associated with organic matter and the divisor in the ratio, and supporting the shoaling of organic matter with these elements during the transgression in each of the events.

Since Wignall and Twitchett (1996) established a threshold by which $Th/U < 2$ indicates anoxic environments of deposition, and $2 < Th/U < 7$ points to oxic conditions, high Th/U values at the NL1, NL2, and HERB events (Fig. 6) seem to be contrary to the I/(Ca+Mg) ratio and what is expected during transgression. However, potential explanations follow. Increments in Th/U can be due to high Th concentrations, low U concentrations, or both. Low U might have its cause in relatively less anoxic conditions and a decrease in the sequestration of U in the sediments during the mentioned minor drops in the sea level. A fall in the sea level delivers shallow waters to deeper settings and, within a more oxygenated water column, the organic matter associated with U has fewer chances of preservation. Therefore, lack of U and, consequently, high Th/U could be recording a relatively shallower

signature within the main transgression, compatible with the dysoxic conditions indicated by the I/(Ca+Mg) ratio values and the higher $\delta^{66}Zn$ (but generally decreasing), caused by some biological uptake. Relatively low U has been also associated to slow bottom water renewal due to partial restriction of local basins (Algeo and Tribovillard, 2009; Li et al., 2022), which is compatible with the presence of micro-continents separated from the Laurentian margin by the Taconic Seaway during the Furongian (White and Waldron, 2022).

Particularly during the HERB event, there is the possibility that thorium addition was sourced by terrigenous inputs, as the positive shift in the Th/U behaves fairly parallel to its Al/Ti and ∑REE counterparts. During a generally warm and humid climate that favoured transgression (increase in Al/Ti), chemical weathering and runoff could have provided clays to the ocean. Continental crust-derived sediments have an average concentration of 10.7 ppm for Th and 2.9 ppm for U (Taylor and McLennan, 1980c; Taylor and McLennan, 1985), meaning that the expected ratio would be around 4. As the higher positive peaks in this section approach these values, crustal influence constitutes an option for high Th/U and is coherent with reducing I/(Ca+Mg) ratios supporting a rise in sea level. It is also compatible with the decreasing isotopic Zn signature affected by both the inhibition of primary productivity by more reducing conditions and lighter isotopic crustal values.

It has been shown that, in reducing systems with considerable depths, Th tends to be absorbed by algae, whereas U is less likely to bind with carbonate ions, resulting in higher Th/U values (Shao et al., 2017). Therefore, considering the incursion of more reducing waters with the rise of sea level along each of the events, this setting could be an alternative explanation for the Th/U positive shifts.

Another factor affecting Th is its enhanced uptake onto particle matter surfaces, controlled by primary productivity near the water surface (Clegg and Whitfield, 1990).

Particles comprise two size fractions, small non-sinking and large sinking particles. The burial of these last ones can translate into higher Th/U ratios. Taking this into account, a greater proportion of Th is possible in association with the minor drops in the sea level and the Martin Point carbonates could be partially recording the shallow environment signature. Thus, the Th/U variations are still consistent with the general dysoxic conditions suggested by the other proxies.

The Ce/Ce* acts as a proxy for variations in redox conditions as well (German and Elderfield, 1990), reaching values towards unity in dysoxic/anoxic conditions, while in relatively more oxic environments it is sequestered to form Mn oxides and hydroxides, and values are usually less than 1. In this study, high Ce anomaly values of 0.92 ± 0.06 (post-SPICE; Table 1) and 0.85 ± 0.07 (HERB; Table 1), suggest dysoxic conditions consistent with the low I/(Ca+Mg) ratios. Cambrian carbonates with similar Ce/Ce* values have also been interpreted as deposited under anoxic-dysoxic water (0.71–0.92; Ling et al., 2013). This supports generally transgressive settings throughout the investigated events, as inferred from the profiles. Nevertheless, the Ce anomaly is a better tracer for oxic conditions than dysoxic (Toslevin et al., 2016) and, thus, it is only utilized here to complement the other proxies.

Chapter VI

Conclusions

Petrographic and geochemical screening support the preservation of at least near-primary signatures of the Zn-isotope compositions, I/(Ca+Mg) ratios and trace elements of the Upper Cambrian lime mudstones of the toe-of-slope rhythmites at Martin Point, western Newfoundland. The signatures are therefore reliable proxies to study variations in the carbonates and their paleoenvironment.

The profiles of $\delta^{66}Zn$ values, I/(Ca+Mg) and trace elements exhibit consistent variations in association with previously studied global negative $\delta^{13}C_{carb}$ shifts (NL1, NL2 and HERB). The low and decreasing Zn-isotope compositions during each of the events reflect inhibition of bioproductivity caused by the shoaling of organic-rich anoxic waters during transgression. Shoaling produced the delivery and emplacement of organic matter with trace elements, resulting in positive shifts in the TOC, P, Ni, Cu, Mn, Fe, REE, V, and Mo profiles. The Al/Ti ratio consistently points to humid and warm climate periods at the NL1, NL2, and HERB events.

On the contrary, minor positive shifts in the $\delta^{66}Zn$ profile throughout the studied interval are associated with a certain degree of bioproductivity and preferential carbonate weathering, due to relative water oxygenation and exposure of carbonate related to episodic and minor drops in the sea level during the main course of transgression.

The low I/(Ca+Mg) ratios indicate dysoxic conditions along the section, consistent with a transgression and a warm, humid climate context. The Mn/Al, Fe/Al, V, Mo, Th/U and Ce/Ce* proxies reinforce this interpretation.

References

Acharya, S.S., Panigrahi, M.K., Gupta, A.K. and Tripathy, S., 2015. Response of trace metal redox proxies in continental shelf environment: The Eastern Arabian Sea scenario. Continental Shelf Research, 106, 70-84.

Allen, J.S., Thomas, W.A. and Lavoie, D., 2010. The Laurentian margin of northeastern North America. The Geological Society of America, Memoir 206, 71-90.

Algeo, T. J. and Lyons, T. W., 2006. Mo-total organic carbon covariation in modern anoxic marine environments: Implications for analysis of paleoredox and paleohydrographic conditions. Paleoceanography 21, PA1016.

Algeo, T. J. and Maynard, J. B., 2004. Trace-element behaviour and redox facies in core shales of Upper Pennsylvanian Kansas-type cyclothems. Chemical Geology 206, 289-318.

Algeo, T. J., and Tribovillard, N., 2009. Environmental analysis of paleoceanographic systems based on molybdenum-uranium covariation. Chemical Geology 268, 211-225.

Anbar, A. D., Duan, Y., Lyons, T. W., Arnold, G. L., Kendall, B., Creaser, R. A., Kaufman, A. J., Gordon, G. W., Scott, C. and Buick, R., 2007. A whiff of oxygen before the Great Oxidation Event? Science vol. 317, issue 5846, 1903-1906. Archer, C., Andersen, M.B., Cloquet, C., Conway, T.M., Dong, S., Ellwood, M., Moore, R., Nelson, J., Rehkämper, M., Rouxel, O. and Samanta, M., 2017. Inter-calibration of a proposed new primary reference standard AA-ETH Zn for zinc isotopic analysis. Journal of Analytical Atomic Spectrometry, 32(2), 415-419.

Azmy, K., 2019a. Carbon-isotope stratigraphy of the uppermost Cambrian in eastern Laurentia: implications for global correlation. Geological Magazine 156 (5), 2019, 759–771.

Azmy, K., 2019b. Carbon-isotope stratigraphy of the SPICE event (Upper Cambrian) in eastern Laurentia: implications for global correlation and a potential reference section. Geological Magazine 156, 1311–1322.

Azmy, K., Brand, U., Sylvester, P. Gleeson, S.A., Logan, A. and Bitner, M.A., 2011. Biogenic and abiogenic low-Mg calcite (bLMC and aLMC): Evaluation of seawater-Ree composition, water masses and carbonate diagenesis. Chemical Geology 280, 180-190.

Babcock, L.E., Peng, S.C., Brett, C.E., Zhu, M.Y., Ahlberg, P., Bevis, M. and Robison, R.A., 2015. Global climate, sea level cycles, and biotic events in the Cambrian Period. Palaeoworld, 24(1-2), 5-15.

Bagnoli, G., Barnes, C.R. and Stevens, R.K., 1986. Lower Ordovician (Tremadocian) conodonts from Broom Point and Green Point, Western Newfoundland. Bollettino della Societá Paleontologica Italiana, 25(2), 145-158 (printed in 1987).

Barnes, C.R., 1988. The proposed Cambrian-Ordovician global boundary stratotype and point (GSSP) in Western Newfoundland, Canada. Geol. Mag. 125 (4). 1988, 381-414.

Bau, M. and Dulski, P., 1996. Distribution of yttrium and rare-earth elements in the Penge and Kuruman iron-formations, Transvaal Supergroup, South Africa. Precambrian Research 79, 37-55.

Bermin, J., Vance, D., Archer, C. and Statham, P. J., 2006. The determination of the isotopic composition of Cu and Zn in seawater. Chem. Geol. 226 (3–4), 280–297.

Bouma, A.H., 1962. Sedimentology of some flysch deposits. Elsevier, Amsterdam, 168.

Böning, P., Brumsack, H-J., Schnetger, B. and Grunwald, M., 2009. Trace element signatures of Chilean upwelling sediments at ~ 36°S. Marine Geology, 259 (1-4), 112-121.

Bowman, C.N., Them, T.R., Knight, M.D., Kaljo, D., Eriksson, M.E., Hints, O., Martma, T., Owens, J.D., Young, S.A. 2021. A multi-proxy approach to constrain reducing

conditions in the Baltic Basin during the late Silurian Lau carbon isotope excursion. Palaeogeography, Palaeoclimatology, Palaeoecology 581, 110624.

Brand, U. and Veizer, J., 1980. Chemical diagenesis of a multicomponent carbonate system; 1, Trace elements. Journal of Sedimentary Research, 50(4), 1219-1236.

Breit, G. N. and Wanty, R. B., 1991. Vanadium accumulation in carbonaceous rocks: a review of geochemical controls during deposition and diagenesis. Chemical Geology, 91(2), 83-97.

Broecker, W. S. and Peng, T. H., 1982. Tracers in the Sea. Eldigio, Pallisades, NY, 690.

Bruland, K. W., 1980. Oceanographic distributions of cadmium, zinc, nickel and copper in the North Pacific. Earth and Planetary Science Letters 47, 176-198.

Brumsack, H. J., 2006. The trace metal content of recent organic carbon-rich sediments: implications for Cretaceous black shale formation. Palaeogeography, Palaeoclimatology, Palaeoecology, 232(2-4), pp.344-361.

Brumsack, H. J. and Gieskes, J. M., 1983. Interstitial water trace-metal chemistry of laminated sediments from the Gulf of California, Mexico. Marine Chemistry, 14(1), 89-106.

Bunzel, D., Schmiedl, G., Lindhorst, S., Mackensen, A., Reolid, J., Romahn, S. and Betzler, C., 2017. A multi-proxy analysis of Late Quaternary ocean and climate variability for the Maldives, Inner Sea. Climate of the Past, 13(12), 1791-1813.

Cawood, P.A., McCausland, P.J.A. and Dunning, G.R., 2001. Opening Iapetus: Constraints from the Laurentian margin in Newfoundland. GSA Bulletin v. 113, No. 4, 443–453.

Canfield, D. E., 1993. Organic Matter Oxidation in Marine Sediments. In: Wollast, R., Mackenzie, F.T., Chou, L. (eds) Interactions of C, N, P and S Biogeochemical Cycles and Global Change. NATO ASI Series, vol 4. Springer, Berlin, Heidelberg.

Canfield, D. E., 1994. Factors influencing organic carbon preservation in marine sediments. Chemical Geology 114, 315-329.

Chapman, J. B., Mason, T. F. D, Weiss, D. J., Coles, B. J., and Wilkinson, J. J., 2006. Chemical separation and isotopic variations of Cu and Zn from five geological reference materials, Geostand. Geoanal. Res. 30 (1), 5–16.

Chen, G., Gang, W. Z., Wang, N. and Zhao, L. Y., 2017. Geochemical characterisation of the Xiagou Formation carbonate-bearing mudstone in southwestern Jiuquan Basin, China: implications for paleoenvironment reconstruction and the origin of organic matter. Australian Journal of Earth Sciences, DOI: 10.1080/08120099.2018.1399926

Chen, J., Geillardet, J., and Louvat, P., 2008. Zinc isotopes in the Seine River waters, France: A probe of anthropogenic contamination: Environmental Science & Technology 42, 6494–6501.

Chen, D., Qing, H. and Li, R., 2005. The Late Devonian Frasnian–Famennian (F/F) biotic crisis: Insights from δ13Ccarb, δ13Corg and 87Sr / 86Sr isotopic systematics. Earth and Planetary Science Letters 235 (1-2), 151-166.

Chen, X., Sageman, B.B., Yao, H., Liu, S.A., Han, K., Zou, Y. and Wang, C., 2021. Zinc isotope evidence for paleoenvironmental changes during Cretaceous Oceanic Anoxic Event 2. Geology, 49(4), 412-416.

Clarkson, M.O., Poulton, S.W., Guilbaud, R. and Wood, R.A., 2014. Assessing the utility of Fe/Al and Fe-speciation to record water column redox conditions in carbonate-rich sediments. Chemical Geology, 382, 111-122.

Clegg, S.L. and Whitfield, M., 1990. A generalized model for the scavenging of trace metals in the open ocean—I. Particle cycling. Deep Sea Research Part A. Oceanographic Research Papers, 37(5), 809-832.

Coniglio, M., 1985. Origin and diagenesis of fine-grained slope sediments: Cow Head Group (Cambro-Ordovician), western Newfoundland. Doctoral (PhD) thesis, Memorial University of Newfoundland.

Cooper, R.A., Nowlan, G.S. and Williams, S.H. 2001. Global Stratotype Section and Point for the base of the Ordovician System. Episodes 24, 19-28.

Cousineau, P.A. and Tremblay, A., 1993. Acadian deformations in the southwestern Quebec Appalachians. In The Acadian Orogeny. Edited by D.C. Roy and J.W. Skehan. Geological Society of America, Special Paper 275, pp. 85–99.

D'Arcy, J., Gilleaudeau, G.J, Peralta, S., Gaucher, C. and Frei, R. 2017. Redox fluctuations in the Early Ordovician oceans: An insight from chromium stable isotopes. Chemical Geology, volume 448, 1-12.

Derry, L.A., Kaufman, A.J. and Jacobsen, S.B., 1992. Sedimentary cycling and environmental change in the Late Proterozoic: evidence from stable and radiogenic isotopes. Geochimica et Cosmochimica Acta, 56(3), 1317-1329.

Dickson, J. A. D. (1966). Carbonate identification and genesis as revealed by staining. Journal of Sedimentary Research, 36(2), 491–505.

Dolenec, T., Lojen, S. and Ramovš, A., 2001. The Permian-Triassic boundary in Western Slovenia (Idrijca Valley section): magnetostratigraphy, stable isotopes, and elemental variations. Chemical Geology 175, 175-190.

Dunham, R.J., 1962. Classification of Carbonate Rocks According to Depositional Texture. In Ham, W.E., Ed., Classification of Carbonate Rocks, AAPG, Tulsa, 108-121.

Edwards, C. T., Fike, D. A., Saltzman, M. R., Lu, W. and Lu, Z., 2018. Evidence for local and global redox conditions at an Early Ordovician (Tremadocian) mass extinction. Earth and Planetary Science Letters 481, 125-135.

Elderfield, H. and Truesdale, V.W., 1980. On the biophilic nature of iodine in seawater. Earth and Planetary Science Letters, 50(1), 105-114.

Emerson, S. R., Huested, S. S., 1991. Ocean anoxia and the concentrations of molybdenum and vanadium in seawater. Mar. Chem. 34, 177–196.

Fantle, M. S., Barnes, B.D. and Lau, K.V., 2020. The role of diagenesis in shaping the geochemistry of the marine carbonate record. Annu. Rev. Earth Planet. Sci. 48:549-83.

Fuge, R. and Johnson, C.C. 1986. The geochemistry of iodine—a review. Environ. Geochem. Health 8, 31–54.

Gao, P., Liu, G., Jia, C., Young, A., Wang, Z., Wang, T., Zhang, P. and Wang, D., 2016. Redox variations and organic matter accumulation on the Yangtze carbonate platform during Late Ediacaran–Early Cambrian: constraints from petrology and geochemistry. Palaeogeography, Palaeoclimatology, Palaeoecology, 450, 91-110.

Gao, Y., Arimoto, R., Duce, R.A., Lee, D.S. and Zhou, M.Y., 1992. Input of atmospheric trace elements and mineral matter to the Yellow Sea during the spring of a low-dust year. Journal of Geophysical Research: Atmospheres, 97(D4), 3767-3777.

Gao, Y., Zhang, X., Xu, Y., Fang, C., Gong, Y. and Shen, Y., 2020. High primary productivity during the Ediacaran Period revealed by the covariation of paired C-isotopic records from South China. Precambrian Research, 349, 105411.

German, C. R. and Elderfield, H., 1990. Application of the Ce anomaly as a paleoredox indicator: the ground rules. Paleoceanography 5, 823-833.

Gill, B. C., Lyons, T. W., Young, S. A., Kump, L. R., Knoll, A. H. and Saltzman, M. R., 2011. Geochemical evidence for widespread euxinia in the Later Cambrian ocean. Nature 469, 80-83.

Han, Z., Hu, X., Hu, Z., Jenkyns, H. C., and Su, T., 2022. Geochemical evidence from the Kioto Carbonate Platform (Tibet) reveals enhanced terrigenous input and deoxygenation during the early Toarcian. Global and Planetary Change 215, 103887.

Hardisty, D.S., Lu, Z., Bekker, A., Diamond, C.W., Gill, B.C., Jiang, G., Kah, L.C., Knoll, A.H., Loyd, S.J., Osburn, M.R. and Planavsky, N.J., 2017. Perspectives on Proterozoic surface ocean redox from iodine contents in ancient and recent carbonate. Earth and Planetary Science Letters, 463, 159-170.

Hardisty, D.S., Lu, Z., Planavsky, N.J., Bekker, A., Philippot, P., Zhou, X. and Lyons, T.W., 2014. An iodine record of Paleoproterozoic surface ocean oxygenation. Geology, 42(7), 619-622.

Hohl, S.V., Becker, H., Herzlieb, S. and Guo, Q., 2015. Multiproxy constraints on alteration and primary compositions of Ediacaran deep-water carbonate rocks, Yangtze Platform, South China. Geochimica et Cosmochimica Acta 163, 262-278.

Holser, W. T., 1997. Evaluation of the application of rare-earth elements to paleoceanography. Palaeogeography, Palaeoclimatology, Palaeoecology, 132(1-4), 309-323.

Hu, Q., Zhao, P., Moran, J. E., Seaman, J. C., 2005. Sorption and transport of Iodine species in sediments from the Savannah River and Hanford Sites. J. Contam. Hydrol., 78, 185-205.

Hubert, J.F., Suchecki, R.K. and Callahan, R.K.M., 1977. The Cow Head Breccia: Sedimentology of the Cambro-Ordovician continental margin, Newfoundland. Soc. Econ. Paleontol. Mineral., Spec. Publ., 25: 125--154.

James, N.P. and Stevens, P.K., 1986. Stratigraphy and correlation of the Cambro-Ordovician Cow Head Group, western Newfoundland. Geological Survey of Canada Bulletin 366, 1–143.

James, N.P., Stevens, R.K., Barnes, C. R. and Knight, I., 1989. A lower Paleozoic continental margin carbonate platform, northern Canadian Appalachians. In: Crevello P.D., Wilson J.L., Sarg J.F. and Read J.F. (eds) Controls on Carbonate Platform and Basin Development. Society of Economic Palaeontologists and Mineralogists, Special Publications, 44, 123- 146.

John, S. G. and Conway, T. M., 2014. A role for scavenging in the marine biogeochemical cycling of zinc and zinc isotopes. Earth Planet. Sci. Lett. 394, 159–167.

John, S.G., Kunzmann, M., Townsend, E.J. and Rosenberg, A.D., 2017. Zinc and cadmium stable isotopes in the geological record: A case study from the post-snowball Earth Nuccaleena cap dolostone. Palaeogeography, Palaeoclimatology, Palaeoecology, 466, 202-208.

Kasemann, S.A., Schmidt, D.N., Bijma, J., Foster, G.L., 2009. *In situ* boron isotope analysis in marine carbonates and its application for foraminifera and palaeo-pH. Chemical Geology volume 260, issues 1-2, 138-147.

Kindle, C.H., and Whittington, H.B., 1958. Stratigraphy of the Cow Head region, western Newfoundland. GSA Bulletin 69 (3), 315-342.

Kunzmann, M., Halverson, G.P., Sossi, P.A., Raub, T.D., Payne, J.L. and Kirby, J., 2013. Zn isotope evidence for immediate resumption of primary productivity after snowball Earth. Geology Geology 41 (1), 27–30.

Lacombe, R.A., Waldron, J.W.F., Williams, S.H. and Harris, N.B., 2019. Melanges and disrupted rocks at the leading edge of the Humber Arm Allochthon, W. Newfoundland Appalachians: Deformation under high fluid pressure. Gondwana Research 74, 216-236.

Landing, E., 2012. The great American carbonate bank in eastern Laurentia: Its births, deaths, and linkage to paleooceanic oxygenation (Early Cambrian–Late Ordovician).

Leverenz, H.W., 1950. Introduction to the Luminescence of Solids. Wiley, New York, 340.

Li, X., Jenkyns, H.C., Wang, C., Hu, X., Chen, X., Wei, Y., Huang, Y. and Cui, J., 2006. Upper Cretaceous carbon- and oxygen-isotope stratigraphy of hemipelagic carbonate facies from southern Tibet, China. Journal of the Geological Society, London 163, 375–82.

Li, D., Zhang, X., Chen, K., Zhang, G., Chen, X., Huang, W., Peng, S. and Shen, Y., 2017. High-resolution C-isotope chemostratigraphy of the uppermost Cambrian stage (Stage 10) in South China: implications for defining the base of Stage 10 and palaeoenvironmental hange. Geological Magazine 154, 1232–43.

Li, D., Zhang, X., Zhang, X., Zhu, H., Peng, S., Sun, L., and Shen, Y., 2020. A paired carbonate-organic $\delta^{13}C$ approach to understanding the Cambrian Drumian carbon isotope excursion (DICE). Precambrian Research 349, 105503.

Li, J., Azmy, K., and Kendall, B., 2022. The Mo- and U-isotope signatures in alternating shales and carbonate beds of rhythmites: A comparison and implications for redox conditions across the Cambrian-Ordovician boundary. Chemical Geology 602, 120882.

Liss, P.S., Herring, J.R., and Goldberg, E.D. 1973. Iodide-iodate system in seawater as a possible measure of redox potential: Nature Physical Science, v. 242, 108–109.

Little, S.H., Vance, D., Walker-Brown, C. and Landing, W.M. 2014 The oceanic mass balance of copper and zinc isotopes, investigated by analysis of their inputs, and outputs to ferromanganese oxide sediments. Geochim. Cosmochim. Acta 125, 673–693.

Little, S.H., Wilson, D.J., Rehkämper, M., Adkins, J.F., Robinson, L.F. and van de Flierdt, T., 2021. Cold-water corals as archives of seawater Zn and Cu isotopes. Chemical Geology, 578, 120304.

Lu, W., Barbosa, C.F., Rathburn, A.E., da Matta Xavier, P., Cruz, A.P.S., Thomas, E., Rickaby, R.E.M, Zhang, Y.G. and Lu, Z., 2021. Proxies for paleo-oxygenation: A downcore comparison between benthic foraminiferal surface porosity and I/Ca. Palaeogeography, Palaeoclimatology, Palaeoecology 579, 110588.

Lu, W., Wörndle, S., Halverson, G. P., Zhou, X., Bekker, A., Rainbird, R. H., Hardisty, D. S., Lyons, T. W., and Lu, Z., 2017. Iodine proxy evidence for increased ocean oxygenation during the Bitter Springs Anomaly. Geochem. Persp. Let. (2017) 5, 53-57

Lu, Z., Hoogakker, B.A.A., Hillenbrand, C.-D., Zhou, X., Thomas, E., Gutchess, K.M., Lu, W., Jones, L. and Rickaby, R.E.M., 2016. Oxygen depletion recorded in upper waters of the glacial Southern Ocean. Nat Commun 7, 11146.

Lu, Z., Jenkyns, H. C. and Rickaby, R. E., 2010. Iodine to calcium ratios in marine carbonate as a paleo-redox proxy during oceanic anoxic events. Geology 38, 1107–1110.

Machel, H.G., 2000. Application of cathodolumisnescence to carbonate diagenesis. Cathodoluminescence in geosciences. Springer, Berlin, Heidelberg, 271-301.

Machel, H.G. and Burton, E.A., 1991. Factors governing cathodoluminescence in calcite and dolomite, and their implications for studies of carbonate diagenesis.

Maréchal, C.N., Nicolas, E., Douchet, C. and Albarede, F., 2000. Abundance of zinc isotopes as a marine biogeochemical tracer. Geochemistry, Geophysics, Geosystems, 1(5).

Maréchal, C.N. and Sheppard, S.M.F., 2002. Isotopic fractionation of Cu and Zn between chloride and nitrate solutions and malachite or smithsonite at 30°C and 50°C. In Goldschmidt Conference. Geochim. Cosmochim. Acta 66, A484.

Maréchal, C.N., Télouk, P. and Albarède, F., 1999. Precise analysis of copper and zinc isotopic compositions by plasma-source mass spectrometry. Chemical geology, 156(1-4), 251-273.

McLennan, S.M., 2001. Relationships between the trace element composition of sedimentary rocks and upper continental crust. Geochemistry, Geophysics, Geosystems, 2(4).

Mavromatis, V., González, A. G., Dietzel, M., Schott, J., 2019. Zinc isotope fractionation during the inorganic precipitation of calcite – Towards a new pH proxy. Geochimica et Cosmochimica Acta 244, 99-112.

Meyer, E. E., Quicksall, A. N., Landis, J. D., Link, P. K. and Bostick, B. C., 2012. Trace and rare earth elemental investigation of a Sturtian cap carbonate, Pocatello, Idaho: evidence for ocean redox conditions before and during carbonate deposition. Precambrian Research, 192, 89-106.

Middelburg, J. J., Van der Weijden, C. H. and Woittiez, J. R. W., 1988. Chemical processes affecting the mobility of major, minor and trace elements during weathering of granitic rocks. Chemical Geology 68, 253-273.

Miller, J.F., Evans, K.R., Freeman, R.L., Ripperdan, R.L. and Taylor, J.F., 2011. Proposed stratotype for the base of the Lawsonian Stage (Cambrian Stage 10) at the first appearance datum of *Eoconodontus notchpeakensis* (Miller) in the House Range, Utah, USA. Bulletin of Geosciences 86, 595–620.

Miller, J.F., Evans, K.R., Loch, J.D., Ethington, R.L., Stitt, J.H., Holmer, L.E. & Popov, L.E. 2003. Stratigraphy of the Sauk III interval (Cambrian–Ordovician) in the Ibex area, western Millard County, Utah. Brigham Young University Geology Studies 47, 23–118.

Millero, F.J., 1996. Chemical Oceanography. CRC Press, Boca Raton, FL, 496.

Morel, F. M. M., Reinfelder, J. R., Chamberlain, C. P., Roberts, S. B., Lee, J. G., Yee, D., 1994. Zinc and carbon co-limitation of marine phytoplankton. Nature 369, 740–742.

Morford, J. L., Emerson, S. R., Breckel, E. J. and Kim, S. H., 2005. Diagenesis of oxyanions (V, U, Re, and Mo) in pore waters and sediments from a continental margin. Geochimica et Cosmochimica Acta, 69 (21), 5021-5032.

Morrison, J.O., and Brand, U., 1986. Geochemistry of recent marine invertebrates. Geoscience Canada, 13, 237–253.

Muramatsu, Y. and Wedepohl, K.H., 1998. The distribution of iodine in the earth's crust. Chemical Geology, 147(3-4), 201-216.

Nakada, R., Takahashi, Y., Tanimizu, M., 2013. Isotopic and speciation study on cerium during its solid-water distribution with implication for Ce stable isotope as a paleo-redox proxy. Geochimica et Cosmochimica Acta, Volume 103, 49-62.

Nakai, S.I., Halliday, A.N. and Rea, D.K., 1993. Provenance of dust in the Pacific Ocean. Earth and Planetary Science Letters, 119(1-2), 143-157.

Niu, J., Huang, W. and Fei, L., 2018. Paleoenvironment in an Ordovician carbonate reservoir in southwestern of Tarin Basin, NW China: Evidence from stable isotopes. Energy Sources, Part A: Recovery, Utilization, and Environmental Effects, 41:16.

Okafor, M-M. C., 2023. Redox conditions across the Upper Cambrian in Western Newfoundland, Canada. Master’s thesis, Memorial University of Newfoundland, Canada.

Palandri, J. L. and Kharaka, Y. K., 2004. A compilation of rate parameters of water-mineral interaction kinetics for application to geochemical modeling. Geological Survey Menlo Park CA.

Pattan, J.N., Mir, I.A., Parthiban, G., Karapurkar, S.G., Matta, V.M., Naidu, P.D. and Naqvi, S.W.A., 2013. Coupling between suboxic condition in sediments of the western Bay of Bengal and southwest monsoon intensification: A geochemical study. Chemical Geology, 343, 55-66.

Pichat, S., Douchet, C., Albarède, F., 2003. Zinc isotope variations in deep-sea carbonates from the eastern equatorial Pacific over the last 175 ka. Earth and Planetary Science Letters 210, 167-178.

Podder, J., Lin, J., Sun, W., Botis, S.M., Tse, J., Chen, N., Hu, Y., Li, D., Seaman, J., Pan, Y., 2017. Iodate in calcite and vaterite: Insights from synchrotron X-ray absorption spectroscopy and first-principles calculations. Geochimica et Cosmochimica Acta 198, 218–228.

Poulton, S.W. and Raiswell, R., 2005. Chemical and physical characteristics of iron oxides in riverine and glacial meltwater sediments. Chemical Geology, 218(3-4), 203-221.

Quinn, L.A., 1992. Foreland and trench slope basin sandstones of the Goose Tickle Group and Lower Head Formation, western Newfoundland. PhD thesis, Memorial University of Newfoundland, St John's, Newfoundland.

Quinn, L., Williams, S.H., Harper, D.A.T. and Clarkson, E.N.K., 1999. Late Ordovician foreland basin fill: Long Point Group of onshore western Newfoundland. Bulletin of Canadian Petroleum Geology, vol. 47, No. 1, 63-80.

Reeder, R.J., Lamble, G.M. and Northrup, P.A., 1999. XAFS study of the coordination and local relaxation around Co^{2+}, Zn^{2+}, Pb^{2+}, and Ba^{2+} trace elements. Am. Miner. 84, 1049-1060.

Rühlemann, C., Frank, M., Hale, W., Mangini, A., Mulitza, S., Müller, P.J. and Wefer, G., 1996. Late Quaternary productivity changes in the western equatorial Atlantic: Evidence from 230Th-normalized carbonate and organic carbon accumulation rates. Marine Geology, 135(1-4), 127-152.

Rostovtseva, Y.V. and Kuleshov, V.N., 2016. Carbon and oxygen stable isotopes in the middle-upper miocene and lower pliocene carbonates of the Eastern Paratethys (Kerch-Taman Region)> Palaeoenvironments and post-sedimentation changes. Lithology and Mineral Resources 51, 333-346.

Rue, E. L., Smith, G. J., Cutter, G. A., Bruland, K. W., 1997. The response of trace element redox couples to suboxic conditions in the water column. Deep-Sea Res., Part 144, 113–134.

Rush, P.F. and Chafetz, H.S., 1990. Fabric-retentive, non-luminescent brachiopods as indicators of original delta 13 C and delta 18 O composition; a test. Journal of Sedimentary Research, 60(6), 968-981.

Sageman, B. B., Murphy, A. E., Werne, J. P., Ver Straeten, C. A., Hollander, D. J. and Lyons, T. W., 2003. A tale of shales: the relative roles of production, decomposition, and dilution in the accumulation of organic-rich strata, Middle–Upper Devonian, Appalachian basin. Chemical Geology, 195(1-4), 229-273.

Scholz, F., Siebert, C., Dale, A.W., Frank, M., 2017. Intense molybdenum accumulation in sediments underneath a nitrogenous water column and implications for the

reconstruction of paleo-redox conditions based on molybdenum isotopes. Geochimica et Cosmochimica Acta volume 213, 400-417.

Shao, L., Cui, Y., Qiao, P., Zhang, D., Liu, X., and Zhang, C., 2017. Sea-level changes and carbonate platform evolution of the Xisha Islands (South China Sea) since the Early Miocene. Palaeogeography, Palaeoclimatology, Palaeoecology. DOI 10.1016/j.palaeo.2017.07.006

Shimura, T., Kon, Y., Sawaki, Y., Hirata, T., Han, J., Shu, D. and Komiya, T., 2014. In-situ analyses of phosphorous contents of carbonate minerals: Reconstruction of phosphorus contents of seawater from the Ediacaran to early Cambrian. Gondwana Research 23 (3), 1090-1107.

Shiller, A. M., and Boyle, E., 1985. Dissolved zinc in rivers. Nature, v. 317, 49-52.

Śliwiński, M.G., Whalen, M.T. and Jed, D.A.Y. 2010 Trace element variations in the Middle Frasnian Punctata Zone (Late Devonian) in the Western Canada sedimentary basin–changes in oceanic bioproductivity and paleoredox spurred by a pulse of terrestrial afforestation?. Geologica Belgica 13/4, 459-482.

Spears, D. A. and Kanaris-Sotiriou, R., 1976. Titanium in some Carboniferous sediments from Great Britain. Geochimica et Cosmochimica Acta, 40(3), 345-351.

Spokes, L. J. and Liss, P. S., 1996. Photochemically induced redox reactions in seawater, II. Nitrogen and iodine. Marine chemistry, 54(1-2), 1-10.

Stenzel, S.R., Knight, I. and James, N.P., 1990. Carbonate platform to foreland basin: Revised stratigraphy of the Table Head Group (Middle Ordovician), western Newfoundland. Canadian Journal of Earth Sciences, v. 27, 14–26.

Stevens, R.K., 1970. Cambro-Ordovician flysch sedimentation and tectonics in west Newfoundland and their possible bearing on a proto-Atlantic Ocean; Flysch Sedimentology in North America, Geological Association of Canada, Special Paper 7, 165-177.

Stitt, J. H, 1977. Late Cambrian and earliest Ordovician trilobites, Wichita Mountains, Murray County, Oklahoma. Oklahoma Geological Survey Bulletin 124, 79.

Stow, D. and Shanmugam, G., 1980. Sequence of structures in fine-grained turbidites: Comparison of recent deep-sea and ancient flysch sediments. Sedimentary Geology, 25, 23-42.

Stouge, S., Bagnoli, G. and McIlroy, D., 2017. Cambrian – Middle Ordovician platform-slope stratigraphy, palaeontology and geochemistry of western Newfoundland, Canada. International Symposium on the Ediacaran-Cambrian Transition, Field Trip 2.

Truesdale, V.W. and Bailey, G.W., 2000. Dissolved iodate and total iodine during an extreme hypoxic event in the Southern Benguela system. Estuarine, Coastal and Shelf Science, 50(6), 751-760.

Taylor, S. R. and McLennan, S. M., 1980c. Rare earth element evidence for the chemical composition of the Archaean crust. Proc. 2nd Int. Archaean Symp., Perth, W.A. I*n* McLennan, S.M., Nance, W.B. and Taylor, S.R., 1980. Rare earth element-thorium correlations in sedimentary rocks, and the composition of the continental crust. Geochimica et Cosmochimica Acta, 44(11), 1833-1839.

Taylor, S. R., and McLennan, S. M., 1985. The continental crust: Its composition and evolution. Blackwell, Malden, Mass.

Tribovillard, N., Algeo, T.J., Baudin, F. and Riboulleau, A., 2012. Analysis of marine environmental conditions based on molybdenum–uranium covariation—Applications to Mesozoic paleoceanography. Chemical Geology, 324, 46-58.

Veizer, J. 1983 Chemical diagenesis of carbonates: theory and application of trace elements technique. In: Arthur, M.A., Anderson, T.F., Kaplan, I.R., Veizer, J., Land, L. S. (Eds.), Stable Isotopes in Sedimentary Geology, vol. 10. Society of Economic Paleontologists and Mineralogists (SEPM), Short course Notes, pp. 3.1–3.100.

Ver Straeten, C. A., Brett, C. E. and Sageman, B. B., 2011. Mudrock sequence stratigraphy: A multi-proxy (sedimentological, paleobiological and geochemical) approach, Devonian Appalachian Basin. Palaeogeography, palaeoclimatology, palaeoecology 304 (1-2), 54-73.

Voegelin, A. R., Nägler, T. F., Samankassou, E. and Villa, I. M., 2009. Molybdenum isotopic composition of modern and Carboniferous carbonates. Chemical Geology 265 (3-4), 488-498.

Waldron, J.W.F., Anderson, S.D., Cawood, P.A., Goodwin, L.B., Hall, J., Jamieson, R.A., Palmer, S.E., Stockmal, G.S. and Williams, P.F., 1998. Evolution of the Appalachian Laurentian margin: Lithoprobe results in western Newfoundland. Can. J. Earth Sci. 35: 1271–1287

Waldron, J.W.F. and Palmer, S.E., 2000. Lithostratigraphy and structure of the Humber Arm Allochthon in the type area, Bay of Islands, Newfoundland. Newfoundland Department of Mines and Energy, Geological Survey, Report 2000-1, 279-290.

Wang, L., Azmy, K., 2020. Palaeoenvironmental changes in slope carbonates across the late cambrian–early ordovician in western Newfoundland. Geol. J. 55 (5), 1–13.

Wang, L., Hu, W., Wang, X., Cao, J. and Yao, S. 2020 Halogens (Cl, Br, and I) geochemistry in Middle Triassic carbonates: Implications for salinity and diagenetic alteration of I/(Ca+Mg) ratios. Chemical Geology 533, 119444.

Wang, X., Liu, S-A., Wang, Z., Chen, D. and Zhang, L., 2018. Zinc and strontium isotope evidence for climate cooling and constraints on the Frasnian-Famennian (~372 Ma) mass extinction. Palaeogeography, Palaeoclimatology, Palaeoecology 498, 68-82.

Wei, G., Liu, Y., Li, X., Shao, L. and Liang, X., 2003. Climatic impact on Al, K, Sc and Ti in marine sediments: evidence from ODP Site 1144, South China Sea. Geochemical Journal, 37(5), 593-602.

White, S. E. and Waldron, J. W. F., 2018. Inversion of Taconian extensional structures during Paleozoic orogenesis in western Newfoundland. *In* Wilson R.W., Houseman G.A., McCaffrey K.J.W., Doré A.G. and Buiter S.J.H. (eds) Fifty Years of the Wilson Cycle Concept in Plate Tectonics. Geological Society, London, Special Publications, 470.

White, S. E., and Waldron, J. W. F., 2022. Along-strike variations in the deformed Laurentian margin in the North Appalachians: Role of inherited margin geometry and colliding archs. Earth-Science Reviews 226, 103931.

Williams, H., 1978. Tectonic Lithofacies Map of the Appalachian Orogen, Map No. 1A; International Geological Correlation Program, Project No. 27, The Appalachian-Caledonides Orogen, Canadian Contribution No. 5.

Williams, S.H., 1997. Graptolites, acritarchs and scolecodonts at Green Point, western Newfoundland: International Cambrian-Ordovician Boundary Working Group, Circular January 1997, 6-15.

Williams, H. and Hiscott, R.N., 1987. Definition of the Iapetus rift-drift transition in western Newfoundland. Geology, v. 15, 1044-1047.

Wignall, P. B. and Twitchett, R. J., 1996. Ocean anoxia and the end-Permian mass extinction. Science 272, 1155-1158.

Won, M. and Iams, W.J., 2002. Late Cambrian radiolarian faunas and biostratigraphy of the Cow Head Group, western Newfoundland. The Paleontological Society, Journal of Paleontology, 76(1), 1-33.

Wong, G.T.F., and Brewer, P.G. 1977. Marine chemistry of iodine in anoxic basins: Geochimica et Cosmochimica Acta, v. 41, 151–159.

Wong, G. T. F., Piumsonboon, A. U., and Dunstan, W. M., 2018. The transformation of iodate to iodide in marine phytoplankton cultures. Marine Ecology Progress Series, vol. 237, 27-39, 2002.

Wörndle, S., Crockford, P.W., Kunzmann, M., Bui, T.H. and Halverson, G.P. 2019 Linking the Bitter Springs carbon isotope anomaly and early Neoproterozoic oxygenation through I/(Ca+Mg) ratios. Chemical Geology 524, 119-135.

Yan, B., Zhu, X., He, X., Tang, S., 2019. Zn isotopic evolution in early Ediacaran ocean: a global signature. Precambrian Research 320, 472-483.

Yarincik, K.M., Murray, R.W. and Peterson, L.C., 2000. Climatically sensitive eolian and hemipelagic deposition in the Cariaco Basin, Venezuela, over the past 578,000 years: Results from Al/Ti and K/Al. Paleoceanography, 15(2), 210-228.

Young, S. A., Kleinberg, A. and Owens, J. D., 2019. Geochemical evidence for expansion of marine euxinia during an early Silurian (Llandovery-Wenlock boundary) mass extinction. Earth and Planetary Science Letters 513, 187-196.

Zhang, S. and Barnes, C.R., 2004. Late Cambrian and Early Ordovician conodont communities from platform and slope facies, western Newfoundland: a statistical approach. Geological Society, London, Special Publications, 230, 47-72.

Zhao, M., Tarhan, L.G., Zhang, Y., Hood, A., Asael, D., Reid, R.P, Planavsky, N.J., 2021. Evaluation of shallow-water carbonates as a seawater zinc isotope archive. Earth and Planetary Science Letters 553, 116599.

Zhao, M-Y. and Zheng, Y-F., 2014. Marine carbonate records of terrigenous input into Paleotethyan seawater: Geochemical constraints from Carboniferous limestones. Geochimica et Cosmochimica Acta 141, 508-531.

Zhao, Y., Vance, D., Abouchami, W., De Baar, H.J.W., 2014. Biogeochemical cycling of zinc and its isotopes in the Southern Ocean: Geochimica et Cosmochimica Acta, v. 125, 653–672, doi:10.1016/j.gca.2013.07.045.

Zhao, Z., Ahlberg, P., Thibault, N., Dahl, T. W., Schovsbo, N. H., and Nielsen, A. T., 2022. High-resolution carbon isotope chemistratigraphy of the middle Cambrian to lowermost Ordovician in southern Scandinavia: Implications for global correlation. Global and Planetary Change, v. 209, 103751.

Zhou, X, Jenkyns, H.C., Owens, J.D., Junium, C.K., Zheng, X-Y., Sageman, B.B., Hardisty, D.S., Lyons, T.W., Ridgwell, A. and Lu, Z. 2015. Upper ocean oxygenation dynamics from I/Ca ratios during the Cenomanian-Turonian OAE 2. Paleoceanography, 30, 510–526.

Zhou, L., Algeo, T.J., Shen, J., Hu, Z., Gong, H., Xie, S., Huang, J. and Gao, S., 2015. Changes in marine productivity and redox conditions during the Late Ordovician Hirnantian glaciation. Palaeogeography, Palaeoclimatology, Palaeoecology, 420, 223-234.

Appendix

Table A1. Elemental and isotopic geochemical compositions of the investigated carbonates at the Martin Point section in western Newfoundland. The highlighted values are from Wang and Azmy (2020). The $\delta^{13}C$ profile is reproduced from Azmy (2019a, b). The TOC data of post-SPICE from Okafor (2023).

Sample ID	$\delta^{13}C$ (‰) VPDB	TOC (%)	$\delta^{66}Zn$ (‰) JMC-Lyon	I (ppm)	Ca (ppm)	Mg (ppm)	Zn (ppm)	Sr (ppm)	P (ppm)	Ni (ppm)	Cu (ppm)	Mn (ppm)	Fe (ppm)	Al (ppm)	V (ppm)	Mo (ppm)	Ti (ppm)	Th (ppm)	U (ppm)	La (ppm)	Ce (ppm)	Pr (ppm)	Nd (ppm)	Sm (ppm)	Eu (ppm)	Gd (ppm)	Tb (ppm)	Dy (ppm)	Ho (ppm)	Er (ppm)	Tm (ppm)	Yb (ppm)	Lu (ppm)
HERB																																	
MH1	+0.55	1.43		0.02	393860	4425	0.9	687	126	3.1	6.8	150	1546	1346	4.7	2.7	38	0.58	0.35	6.0	10.3	1.4	4.9	0.9	0.18	0.6	0.09	0.6	0.11	0.30	0.04	0.22	0.04
MH2	+0.07	0.60	+0.26																														
MH3	-0.72	0.99	+0.23	0.08	394512	3955	1.2	536	183	3.6	8.1	335	2478	1668	5.8	1.8	33	0.66	0.41	11.3	20.8	2.2	8.6	1.2	0.29	1.3	0.19	1.2	0.30	0.90	0.12	0.62	0.09
MH4	-0.13	0.54																															
MH5	-0.29	2.71			392852	5151		979.8	251.9	4.1	9.0	253	2747	613.6	2.9	2.7	17	0.24	0.19	10.5	13.3	1.8	6.8	1.0	0.24	0.8	0.12	0.6	0.14	0.33	0.04	0.17	0.05
MH6	-1.14	0.48	+0.31																														
MH7	-1.89	0.83	+0.44	0.0002	394092	4258	2.0	596	85.3	3.9	6.1	271	4604	1785	4.4	1.5	40	0.61	0.22	12.8	20.6	2.4	9.0	1.4	0.30	1.1	0.17	1.0	0.21	0.58	0.09	0.50	0.05
MH8	-1.67																																
MH9	-1.69	0.68	+0.32				3.9	498	123	5.2	7.2	339	4932	1967	5.8	1.9	54	0.85	0.22	13.0	21.7	2.7	9.8	1.6	0.30	1.2	0.17	1.0	0.22	0.60	0.07	0.44	0.07
MH10	-1.70		+0.48	0.03																													
MH11	-1.90	0.64					2.3	233	145	6.3	7.0	433	5201	2672	5.9	4.8	57	2.15	0.43	20.9	33.0	3.9	14.8	2.4	0.56	1.9	0.32	1.7	0.41	0.91	0.21	0.69	0.18
MH12	-0.65	0.57	+0.44	0.31																													
MH13	-1.22	0.30																															
MH14	-1.34																																
MH15	-1.44		+0.43				16.8	187	115	5.4	8.0	572	6900	3202.3	6.4	2.9	40	1.19	0.33	24.5	38.8	4.1	15.7	2.3	0.61	2.3	0.41	2.5	0.62	1.47	0.27	1.27	0.25
MH16	-1.44	0.85																															
MH17	-1.12		+0.43																														
MH18	-0.58	1.67	+0.18	0.05	395659	3128	3.0	216	128	8.5	8.6	387	1326	1038	4.5	3.2	27	0.55	1.98	10.4	19.6	2.2	8.1	1.6	0.33	1.3	0.26	1.4	0.32	0.76	0.14	0.73	0.13
MH19	-0.25	0.99	+0.36	0.18	389691	8157	14.4	165	159	3.7	5.2	438	3852	2400	6.4	1.3	48	0.88	0.97	17.0	26.6	3.1	12.1	2.0	0.45	1.9	0.28	1.8	0.43	1.12	0.18	0.85	0.13
MH20	-1.20																																
MH21	-1.12	0.79		0.24																													
MH22	-0.68	0.88	+0.45																														
MH23	-0.69																																
MH24	-0.56	1.17	+0.38				0.6	238	113	2.7	5.4	228	1074	892	5.1	1.8	28	0.39	0.94	8.2	14.0	1.4	5.9	1.0	0.23	0.8	0.12	0.9	0.16	0.49	0.06	0.40	0.08
MH25	-0.66	0.49																															
MH26	-0.16	1.51																															
MH27	-0.76	0.51																															
MH28	-0.33	0.93																															
MH29	-1.28		+0.33	0.19	395078	3547		218	142	2.7	5.5	562	1465	1103	5.5	1.2	43	0.43	3.57	19.1	33.1	3.5	14.5	2.3	0.54	2.2	0.35	2.4	0.54	1.34	0.20	1.19	0.18
MH30	-1.13																																
MH31	-0.17	3.10	+0.16																														
MH32	+0.21	0.89	+0.34	0.17	394926	3657		231	94	2.4	5.1	183	1027	833	2.4	1.4	22	0.23	0.95	7.4	10.3	1.3	4.6	0.8	0.20	0.6	0.10	0.7	0.11	0.33	0.05	0.25	0.05
MH33	-0.13	0.67																															
MP1	-0.88	0.56																															
MP2	-1.45	0.67	+0.35	0.16	395082	3544		310	86	1.9	12.2	292	1027	820	4.3	1.1	24	0.14	0.82	7.5	10.6	1.2	4.6	0.6	0.16	0.6	0.09	0.6	0.15	0.31	0.05	0.31	0.05
MP3	+0.11	0.98																															
MP4	+0.26																																
MP5	+0.58	2.15		0.34	395916	2943		250	150	2.1	4.7	523	904	681	2.2	1.0	24	0.21	1.60	6.0	9.7	1.1	4.6	0.7	0.19	0.7	0.10	0.6	0.11	0.39	0.05	0.30	0.03
MP6	-0.66	1.11																															
MP7	-0.32	1.29																															
MP8	-1.13	0.71		0.39	389292	7717	21.7	262	205	3.6	6.0	360	2336	1992	7.8	0.8	68	0.58	2.14	15.2	23.6	2.9	11.6	2.1	0.43	1.7	0.21	1.5	0.31	0.80	0.09	0.55	0.09
MP9	-0.52	0.38																															
MP10	+0.46	1.09						247	191	2.3	6.3	569	1019	794	5.5	1.0	31	0.27	0.75	7.3	11.2	1.4	5.6	0.9	0.21	0.6	0.12	0.7	0.15	0.37	0.05	0.25	0.05
MP11	+0.19	1.58																															
MP12	+0.28	1.55																															
MP13	+0.75																																
MP14	+1.00	0.57	+0.09	0.16	395879	2969	1.2	194	116	7.3	17.4	569	785	611	3.4	11.7	32	1.49	2.63	9.1	13.7	1.7	6.2	1.1	0.46	1.0	0.31	1.0	0.41	0.67	0.31	0.56	0.27
MP15	+0.98																																

(cont.)

Sample ID	$\delta^{13}C$ (‰) VPDB	TOC (%)	$\delta^{66}Zn$ (‰) JMC-Lyon	I (ppm)	Ca (ppm)	Mg (ppm)	Zn (ppm)	Sr (ppm)	P (ppm)	Ni (ppm)	Cu (ppm)	Mn (ppm)	Fe (ppm)	Al (ppm)	V (ppm)	Mo (ppm)	Ti (ppm)	Th (ppm)	U (ppm)	La (ppm)	Ce (ppm)	Pr (ppm)	Nd (ppm)	Sm (ppm)	Eu (ppm)	Gd (ppm)	Tb (ppm)	Dy (ppm)	Ho (ppm)	Er (ppm)	Tm (ppm)	Yb (ppm)	Lu (ppm)
Post-SPICE (NL 1 and NL 2)																																
Sample ID																																
B1-3	-1.68	0.43	+0.37		309259	9029	8.1	231	295	8.7	7.8	666	11639	5847	18.8	0.43	120	1.76	3.05	25.5	41.0	4.9	16.7	2.6	0.63	2.7	0.37	1.9	0.37	0.99	0.14	0.89	0.13
B2-1	-3.85		+0.24		343808	9844	18.4	209	572	9.4	6.4	517	14267	4784	13.8	1.18	98	1.47	0.71	33.2	50.5	6.0	20.4	3.0	0.74	3.3	0.44	2.2	0.42	1.06	0.14	0.83	0.12
B2-2	-2.28		+0.34		332864	15595	6.5	230	149	7.9	3.0	659	11842	5770	19.9	0.32	119	1.27	1.11	26.1	42.1	5.0	17.2	2.7	0.70	2.9	0.43	2.4	0.49	1.30	0.18	1.13	0.16
B4-1	-2.40	0.24	+0.14	0.04	381857	2695	4.1	208	106	1.1	0.6	175	1212	1202	4.3	0.04	38	0.28	0.12	4.6	8.0	0.9	3.0	0.4	0.09	0.4	0.05	0.2	0.05	0.12	0.02	0.11	0.02
B6	-1.30	0.20	+0.21	0.40	246336	11351	10.1	263	354	6.7	6.7	343	10298	4886	13.2	0.23	211	2.36	0.53	22.8	42.1	5.2	18.4	2.9	0.60	2.9	0.36	1.7	0.31	0.79	0.11	0.70	0.10
B10	-0.58	0.10	+0.33	0.14	304114	4197	3.6	203	190	3.2	2.0	286	4559	2629	6.7	0.17	40	1.63	1.22	13.4	26.6	2.9	10.6	1.7	0.40	2.0	0.26	1.3	0.26	0.72	0.10	0.68	0.10
B12	-1.38	0.28																														
B14-1	-0.96		+0.28	0.18	307080	7481	9.5	155	304	11.2	5.2	264	7095	5772	19.8	0.61	111	2.76	2.26	12.8	23.9	2.6	9.5	1.5	0.34	1.5	0.19	0.9	0.18	0.47	0.07	0.44	0.06
B14-2	-0.02	0.34	+0.37		338646	3734	2.9	332	160	2.5	1.6	211	2498	1743	6.0	0.13	48	0.93	0.53	18.4	32.5	3.9	13.4	2.0	0.45	2.0	0.26	1.2	0.22	0.57	0.08	0.52	0.08
B14-3	-0.67	0.30	+0.31	0.04	296687	6945	7.1	402	163	9.9	5.5	256	9838	7005	21.9	0.14	222	2.48	0.47	15.4	30.9	3.4	11.9	1.9	0.42	1.8	0.24	1.1	0.22	0.56	0.08	0.50	0.07
B16-1	-0.41																															
B16-3	-0.32	0.18		0.08	265878	7243	10.7	233	384	12.0	7.3	572	11144	11229	39.4	0.29	199	3.06	3.21	33.6	66.6	6.8	25.0	4.0	0.94	4.0	0.55	2.9	0.56	1.50	0.21	1.37	0.20
B18-1	-0.74																															
B18-2			+0.19		330487	2230	2.6	218	264	2.4	1.6	380	2440	1879	6.7	0.14	43	0.94	1.11	30.7	53.6	5.8	20.0	3.0	0.72	3.3	0.46	2.5	0.53	1.50	0.23	1.52	0.23
B19	-0.76	0.17																														
B20-2	-0.48																															
B22-1	-0.42	0.20	+0.26	0.15	351568	2964	2.3	302	45	3.4	2.1	202	2505	1167	2.1	0.06	22	0.46	0.21	6.3	11.5	1.3	4.3	0.7	0.15	0.8	0.09	0.4	0.08	0.22	0.03	0.21	0.03
B22-3	-1.06																															
B22-5	-1.51	0.18	+0.38		309473	11763	3.6	184	151	2.8	2.4	335	7884	2914	9.8	0.46	32	1.20	1.58	17.2	30.6	3.5	12.3	1.9	0.46	2.3	0.30	1.4	0.29	0.80	0.12	0.77	0.11
B23-2	-0.94	1.46																														
B23-3	-1.31																															
B23-6	-1.32		+0.41	0.38	338553	8883	3.4	217	123	3.1	2.3	215	7075	1557	4.7	0.50	43	1.02	0.79	24.9	39.2	4.7	16.1	2.4	0.53	2.8	0.34	1.6	0.31	0.83	0.12	0.79	0.11
B23-9	-0.39	1.25	+0.34	0.17	389269	2188	1.9	992	57	1.5	1.4	134	2147	456	4.6	0.12	19	0.28	1.28	5.2	8.9	0.9	3.0	0.4	0.10	0.5	0.06	0.3	0.06	0.17	0.02	0.15	0.02
B27-1	-0.59																															
B29-3	+0.30	1.76	+0.25	0.388	308687	6788	8.4	513	192	13.5	8.5	125	13711	2975	30.2	1.14	106	2.30	0.95	15.5	29.6	3.4	12.5	2.1	0.48	2.2	0.31	1.6	0.31	0.82	0.12	0.74	0.11
B29-5	-0.07																															
B29-7	-0.79	0.56																														
B31-2	-0.11		+0.36		341107	10279	4.3	205	81	2.7	1.7	177	6889	1544	6.4	0.41	44	1.28	0.66	15.4	28.4	3.2	11.5	1.9	0.43	2.1	0.28	1.3	0.26	0.68	0.10	0.63	0.09
B31-3	+0.27																															
B31-4	+0.70	1.09	+0.23	0.25	391818	6066	7.7	236	130	3.4	3.2	189	4767	2256	5.1	0.38	50	1.16	1.24	10.1	21.5	2.3	8.5	1.4	0.34	1.7	0.23	1.1	0.23	0.60	0.09	0.54	0.08
B31-7																																
B31-9	+0.68	0.94	+0.34		387574	5049	4.0	288	116	1.0	0.8	162	2030	465	1.7	0.40	16	0.41	0.33	21.5	32.5	4.2	14.0	2.2	0.52	2.5	0.33	1.5	0.30	0.75	0.11	0.66	0.09
B31-11	-0.38																															
B32	-0.69	0.50	+0.73	0.04	221926	127353	3.6	121	250	3.2	4.7	491	22550	2678	12.0	0.37	26	1.43	0.68	11.1	20.6	2.3	8.8	1.5	0.36	1.7	0.24	1.1	0.23	0.59	0.08	0.52	0.07
B33-2	+0.96	1.52																														
B35-1	-0.88		+0.58		431121	4698	0.7	220	114	0.7	0.5	149	1402	659	2.2	0.09	12	0.43	1.16	9.3	15.9	1.9	6.9	1.1	0.26	1.3	0.17	0.8	0.17	0.43	0.06	0.36	0.05
B35-3	-1.40	2.98	+0.34	0.32	335460	5112	1.4	418	175	14.3	8.1	235	16553	1463	5.7	3.98	36	1.00	1.183	17.6	35.3	4.2	15.3	2.7	0.61	2.6	0.38	2.0	0.38	0.98	0.14	0.90	0.13
B36a-2	-4.79	0.52	+0.26	0.31	363958	6461	13.0	218	178	4.0	2.1	972	5660	3864	6.5	0.08	32	1.34	0.29	12.9	24.3	2.9	10.5	1.7	0.40	2.0	0.26	1.3	0.26	0.67	0.09	0.59	0.09
B36a-3	-0.80	0.51	+0.19	0.10	270053	5092	29.9	330	479	35.8	19.8	971	56094	7155	20.7	4.79	131	2.38	2.34	30.8	64.8	7.8	29.8	5.3	1.28	5.4	0.80	4.2	0.82	2.11	0.29	1.81	0.26
B36a-4	-1.29	0.53	+0.37		327222	7489	11.0	325	433	13.7	9.9	1005	32478	5363	10.1	1.01	50	2.13	1.95	24.3	50.7	6.2	24.4	4.4	1.09	4.9	0.70	3.5	0.69	1.76	0.24	1.51	0.22
B36a-5	-3.92	0.78																														
B36a-6	-2.66		+0.44	0.31	350454	5014	4.5	221	179	6.3	3.5	1176	7702	6397	10.1	0.20	44	1.89	0.77	16.5	32.9	4.0	15.0	2.4	0.59	2.8	0.38	1.9	0.37	0.97	0.14	0.85	0.12
B36c-1	-0.12		+0.12		393491	8794	40.9	447	227	3.7	2.0	298	7520	3027	5.9	0.42	29	1.10	0.76	17.8	32.0	3.8	14.2	2.4	0.56	2.6	0.35	1.6	0.31	0.76	0.10	0.63	0.09
B36c-2	+0.56																															
B36c-3	+0.32		+0.35	0.28	415615	6989	4.5	663	142	4.0	1.6	251	5940	3913	6.1	0.25	52	1.21	0.46	10.1	20.0	2.5	9.6	1.6	0.40	1.7	0.24	1.1	0.22	0.55	0.08	0.48	0.07
B36c-4	-1.96	0.44	+0.33	0.56	417751	9697	4.2	544	303	3.2	2.9	184	5595	4447	8.3	0.57	50	1.05	0.52	14.5	29.3	3.8	14.7	2.5	0.60	2.7	0.37	1.7	0.32	0.77	0.10	0.64	0.09
B36d-1	-0.72																															
B36d-2	-1.04	0.80	+0.46	0.26	466606	6170	1.8	395	117	2.6	4.9	255	3913	4816	9.5	0.07	41	0.62	0.56	8.1	15.5	1.8	6.6	1.1	0.27	1.2	0.18	0.9	0.20	0.55	0.08	0.53	0.08

Table A2. Summary of the petrographic observations made on the thin sections of the investigated carbonates.

Sample ID	Main texture (Dunham, 1962)	Mud/grain supported	Phases proportions (%)						Observations
			Matrix	Cement	Allochems			Visible porosity	
					Peloids	Ooids	Quartz		
MH1	Mudstone	Mud-supported	98%	-	-	-	-	2% Vuggy	Solution seams
MH2	Mudstone	Mud-supported	81%	10%	3%	-	1%	3% Fracture	Microvein with carbonate cement and quartz, 2% opaque minerals
MH3	Mudstone	Mud-supported	95%	4%	-	-	-	-	Stylolites, 1% opaque minerals
MH4	Mudstone	Mud-supported	99%	-	-	-	-	-	1% opaque minerals
MH5	Mudstone	Mud-supported	84%	10%	-	-	4%	2% Vuggy	Microvein with carbonate cement and quartz
MH6	Mudstone	Mud-supported	99%	-	-	-	-	-	1% opaque minerals
MH7	Mudstone	Mud-supported	99%	-	-	-	-	-	1% opaque minerals
MH8	Mudstone	Mud-supported	95%	5%	-	-	-	-	-
MH9	Mudstone	Mud-supported	82%	7%	5%	-	2%	4% Vuggy	-
MH10	Mudstone	Mud-supported	90%	10%	-	-	-	-	-
MH11	Mudstone	Mud-supported	91%	8%	-	-	-	-	1% organic matter
MH12	Mudstone	Mud-supported	87%	3%	5%	-	1%	2% Fenestral	Stylolites, 2% organic matter
MH13	Wackestone	Mud-supported	81%	3%	10%	-	4%	-	Stylolites, 2% organic matter
MH14	Mudstone	Mud-supported	98%	-	-	-	-	-	Stylolites, 2% organic matter
MH15	Mudstone	Mud-supported	91%	7%	-	-	-	2% Fracture	0.5% organic matter, microfracture
MH16	Mudstone	Mud-supported	94%	2%	-	-	-	4% Fenestral	Microvein with carbonate cement
MH17	Mudstone	Mud-supported	99%	-	-	-	-	-	1% opaque minerals
MH18	Mudstone	Mud-supported	99%	-	-	-	-	-	1% opaque minerals
MH19	Mudstone	Mud-supported	98.5%	-	-	-	-	-	1% opaque minerals, 0.5% organic matter
MH20	Mudstone	Mud-supported	95%	2%	-	-	1%	-	1% organic matter, solutions seams, microvein with carbonate cement, 1% opaque minerals
MH21	Mudstone	Mud-supported	99%	1%	-	-	-	-	Microvein with carbonate cement
MH22	Mudstone	Mud-supported	97.5%	1%	-	-	1%	-	Microvein with carbonate cement, solution seams, 0.5% organic matter
MH23	Mudstone	Mud-supported	95%	5%	-	-	-	-	-
MH24	Mudstone	Mud-supported	99.5%	-	-	-	-	-	0.5% organic matter
MH25	Mudstone	Mud-supported	96%	4%	-	-	-	-	Microveins with carbonate cement
MH26	Mudstone	Mud-supported	97%	3%	-	-	-	-	Microvein with carbonate cement
MH27	Mudstone	Mud-supported	99%	-	-	-	-	-	1% opaque minerals, microveins with carbonate minerals
MH28	Mudstone	Mud-supported	96%	4%	-	-	-	-	1% opaque minerals
MH29	Mudstone	Mud-supported	97%	2%	-	-	1%	-	Microvein with carbonate minerals and quartz
MH30	Packstone	Grain-supported	38.5%	5%	48%	-	3%	-	Stylolites, 1.5% organic matter, 4% opaque minerals

(cont.)

Sample ID	Main texture (Dunham, 1962)	Mud/grain supported	Phases proportions (%)						Observations
			Matrix	Cement	Allochems			Visible porosity	
					Peloids	Ooids	Quartz		
MH31	Mudstone	Mud-supported	86.5%	12%	-	-	-	-	1% opaque minerals, 0.5% organic matter, microveins with carbonate cement
MH32	Mudstone	Mud-supported	90%	7%	-	-	-	3% Fracture	Microveins with carbonate cement, microfractures
MH33	Mudstone	Mud-supported	88%	10%	-	-	-	-	1% opaque minerals, microveins with carbonate minerals, 1% organic matter
MP1	Mudstone	Mud-supported	95%	5%	-	-	-	-	Microveins with carbonate cement
MP2	Mudstone	Mud-supported	95%	5%	-	-	-	-	Microveins with carbonate cement
MP3	Mudstone	Mud-supported	98.5%	-	-	-	-	-	0.5% organic matter, 1% opaque minerals
MP4	Mudstone	Mud-supported	98%	-	-	-	-	2% Vuggy	-
MP5	Mudstone	Mud-supported	98.5%	-	-	-	-	1% Fracture	0.5% organic matter, microfracture
MP6	Mudstone	Mud-supported	97.5%	1%	-	-	-	-	1.5% organic matter, stylolites, microvein with carbonate minerals
MP7	Mudstone	Mud-supported	91%	8%	-	-	-	-	1% opaque minerals
MP8	Mudstone	Mud-supported	99.50%	-	-	-	-	-	0.5% opaque minerals
MP9	Mudstone	Mud-supported	94.50%	5%	-	-	-	-	0.5% opaque minerals
MP10	Mudstone	Mud-supported	97%	-	-	-	-	3% Fracture	Microfractures
MP11	Mudstone	Mud-supported	96%	1.5%	-	-	-	1%	Microveins with carbonate cement, 1.5% organic matter
MP12	Mudstone	Mud-supported	92%	8%	-	-	-	-	-
MP13	Mudstone	Mud-supported	97%	2%	-	-	-	-	Microvein with carbonate cement, 1% organic matter
MP14	Mudstone	Mud-supported	99%	-	-	-	-	1% Fracture	Microfracture
MP15	Mudstone	Mud-supported	99%	1%	-	-	-	-	-
B1-3	Mudstone	Mud-supported	60%	15%	-	-	-	25% Fenestral	Solution seams
B2-1	Mudstone (based on macro scale sample, no thin section)								
B2-2	Mudstone (based on macro scale sample, no thin section)								
B4-1	Mudstone	Mud-supported	94%	5%	-	-	-	-	Microveins with carbonate cement, 1% opaque minerals
B6	Mudstone	Mud-supported	88%	4%	-	-	8%	-	Microveins with carbonate cement
B10	Mudstone	Mud-supported	88%	2%	-	-	10%	-	Quartz microvein
B12	Mudstone	Mud-supported	89%	6%	-	-	3%	2% Fenestral	Quartz and carbonate microvein
B14-1	Mudstone (based on macro scale sample, no thin section)								
B14-2	Mudstone	Mud-supported	92.5%	2%	-	-	1.5%	3% Fenestral	Solution seams, 1% opaque minerals
B14-3	Mudstone (based on macro scale sample, no thin section)								
B16-1	Packstone	Grain-supported	20%	12%	68%		-	3% Intergranular	Microvein with carbonate cement, lithic fragments
B16-3	Mudstone (based on macro scale sample, no thin section)								
B18-1	Mudstone	Mud-supported	98%	1%	-	-	1%	1% Fenestral	-
B18-2	Mudstone (based on macro scale sample, no thin section)								
B19	Mudstone	Mud-supported	81%	2%	-	-	15%	1% Fracture	1% opaque minerals
B20-2	Mudstone	Mud-supported	92%	4%	-	-	1%	2% Fenestral	Microvein with carbonate cement, 1% opaque minerals
B22-1	Mudstone	Mud-supported	94%	5%	-	-	-	-	Microvein with carbonate cement, 1% opaque minerals

(cont.)

Sample ID	Main texture (Dunham, 1962)	Mud/grain supported	Phases proportions (%)						Observations
			Matrix	Cement	Allochems			Visible porosity	
					Peloids	Ooids	Quartz		
B22-3	Mudstone (based on macro scale sample, no thin section)								
B22-5	Mudstone	Mud-supported	77%	2%	-	-	15%	6% Fenestral	-
B23-2	Mudstone	Mud-supported	98.5%	-	-	-	1%	-	0.5% organic matter
B23-3	Mudstone (based on macro scale sample, no thin section)								
B23-6	Wackestone/Packstone	Mud/grain-supported	55%	2%	35%	-	5%	3% Intergranular	-
B23-9	Mudstone	Mud-supported	99%	-	-	-	-	1% Fenestral	Stylolites
B27-1	Wackestone	Mud-supported	59%	4%	30%	-	5%	2% Fenestral	-
B29-3	Mudstone	Mud-supported	98.8%	-	-	-	0.2%	1% Fenestral	-
B29-5	Mudstone	Mud-supported	82%	5%	8%	-	1%	3% Fenestral	1% opaque minerals
B29-7	Mudstone	Mud-supported	98%	-	-	-	1%	1% Fenestral	-
B31-2	Mudstone	Mud-supported	79.5%	20%	-	-	0.5%	-	Microvein with carbonate cement
B31-3	Mudstone (based on macro scale sample, no thin section)								
B31-4	Mudstone	Mud-supported	99.3%	-	-	-	0.2%	0.5% Fenestral	-
B31-7	Wackestone	Mud-supported	52%	25%	10%	-	10%	2% Fenestral	1% opaque minerals
B31-9	Mudstone	Mud-supported	92%	2%	-	-	4%	-	Solution seams, 2% opaque minerals
B31-11	Mudstone	Mud-supported	99%	1%	-	-	-	-	Microvein with carbonate cement
B32	Mudstone	Mud-supported	36.5%	50%	-	-	7.5%	6% Fenestral	Dolomite
B33-2	Mudstone	Mud-supported	99%	-	-	-	-	-	1% organic matter
B35-1	Packstone	Grain-supported	46%	4%	60%	-	1%	-	Stylolites, 1% opaque minerals
B35-3	Packstone	Grain-supported	45%	4%	60%	-	2%	-	Solution seams, microvein with carbonate cement, 1% opaque minerals
B36a-2	Mudstone (based on macro scale sample, no thin section)								
B36a-3	Mudstone	Mud-supported	96.9%	-	-	-	0.1%	-	3% opaque minerals
B36a-4	Mudstone (based on macro scale sample, no thin section)								
B36a-5	Wackestone	Mud-supported	84.8%	-	13%	-	0.2%	-	2% organic matter
B36a-6	Mudstone	Mud-supported	97.8%	-	-	-	0.2%	-	2% opaque minerals
B36c-1	Mudstone	Mud-supported	96%	2%	-	-	-	2% vuggy	Microvein with carbonate cement
B36c-2	Mudstone (based on macro scale sample, no thin section)								
B36c-3	Mudstone (based on macro scale sample, no thin section)								
B36c-4	Mudstone	Mud-supported	90%	10%	-	-	1%	7% vuggy	-
B36d-1	Mudstone (based on macro scale sample, no thin section)								
B36d-2	Mudstone	Mud-supported	100%	-	-	-	-	-	-